PHYSICAL REVIEW C **92**, 034913 (2015)

Systematic study of azimuthal anisotropy in Cu + Cu and Au + Au collisions at $\sqrt{s_{NN}} = 62.4$ and 200 GeV

A. Adare,[11] S. Afanasiev,[27] C. Aidala,[12,39] N. N. Ajitanand,[57] Y. Akiba,[51,52] H. Al-Bataineh,[45] A. Al-Jamel,[45] J. Alexander,[57] K. Aoki,[32,51] L. Aphecetche,[59] R. Armendariz,[45] S. H. Aronson,[6] J. Asai,[52] E. T. Atomssa,[33] R. Averbeck,[58] T. C. Awes,[47] B. Azmoun,[6] V. Babintsev,[21] G. Baksay,[17] L. Baksay,[17] A. Baldisseri,[14] K. N. Barish,[7] P. D. Barnes,[36,*] B. Bassalleck,[44] S. Bathe,[4,7] S. Batsouli,[12,47] V. Baublis,[50] F. Bauer,[7] A. Bazilevsky,[6] S. Belikov,[6,25,*] R. Bennett,[58] Y. Berdnikov,[54] A. A. Bickley,[11] M. T. Bjorndal,[12] J. G. Boissevain,[36] H. Borel,[14] K. Boyle,[58] M. L. Brooks,[36] D. S. Brown,[45] D. Bucher,[40] H. Buesching,[6] V. Bumazhnov,[21] G. Bunce,[6,52] J. M. Burward-Hoy,[36] S. Butsyk,[36,58] S. Campbell,[58] J.-S. Chai,[28] B. S. Chang,[67] J.-L. Charvet,[14] S. Chernichenko,[21] C. Y. Chi,[12] J. Chiba,[29] M. Chiu,[12,22] I. J. Choi,[67] T. Chujo,[63] P. Chung,[57] A. Churyn,[21] V. Cianciolo,[47] C. R. Cleven,[19] Y. Cobigo,[14] B. A. Cole,[12] M. P. Comets,[48] P. Constantin,[25,36] M. Csanád,[16] T. Csörgő,[66] T. Dahms,[58] K. Das,[18] G. David,[6] M. B. Deaton,[1] K. Dehmelt,[17] H. Delagrange,[59] A. Denisov,[21] D. d'Enterria,[12] A. Deshpande,[52,58] E. J. Desmond,[6] O. Dietzsch,[55] A. Dion,[58] M. Donadelli,[55] J. L. Drachenberg,[1] O. Drapier,[33] A. Drees,[58] A. K. Dubey,[65] A. Durum,[21] V. Dzhordzhadze,[7,60] Y. V. Efremenko,[47] J. Egdemir,[58] F. Ellinghaus,[11] W. S. Emam,[7] A. Enokizono,[20,35] H. En'yo,[51,52] B. Espagnon,[48] S. Esumi,[62] K. O. Eyser,[7] D. E. Fields,[44,52] M. Finger,[8,27] M. Finger, Jr.,[8,27] F. Fleuret,[33] S. L. Fokin,[31] B. Forestier,[37] Z. Fraenkel,[65,*] J. E. Frantz,[12,46,58] A. Franz,[6] A. D. Frawley,[18] K. Fujiwara,[51] Y. Fukao,[32,51] S.-Y. Fung,[7] T. Fusayasu,[42] S. Gadrat,[37] I. Garishvili,[60] F. Gastineau,[59] M. Germain,[59] A. Glenn,[11,60] H. Gong,[58] M. Gonin,[33] J. Gosset,[14] Y. Goto,[51,52] R. Granier de Cassagnac,[33] N. Grau,[2,25] S. V. Greene,[63] M. Grosse Perdekamp,[22,52] T. Gunji,[10] H.-Å. Gustafsson,[38,*] T. Hachiya,[20,51] A. Hadj Henni,[59] C. Haegemann,[44] J. S. Haggerty,[6] M. N. Hagiwara,[1] H. Hamagaki,[10] R. Han,[49] H. Harada,[20] E. P. Hartouni,[35] K. Haruna,[20] M. Harvey,[6] E. Haslum,[38] K. Hasuko,[51] R. Hayano,[10] X. He,[19] M. Heffner,[35] T. K. Hemmick,[58] T. Hester,[7] J. M. Heuser,[51] H. Hiejima,[22] J. C. Hill,[25] R. Hobbs,[44] M. Hohlmann,[17] M. Holmes,[63] W. Holzmann,[57] K. Homma,[20] B. Hong,[30] T. Horaguchi,[51,61] D. Hornback,[60] S. Huang,[63] M. G. Hur,[28] T. Ichihara,[51,52] H. Iinuma,[32,51] K. Imai,[26,32,51] M. Inaba,[62] Y. Inoue,[51,53] D. Isenhower,[1] L. Isenhower,[1] M. Ishihara,[51] T. Isobe,[10] M. Issah,[57] A. Isupov,[27] B. V. Jacak,[58] J. Jia,[12] J. Jin,[12] O. Jinnouchi,[52] B. M. Johnson,[6] K. S. Joo,[41] D. Jouan,[48] F. Kajihara,[10,51] S. Kametani,[10,64] N. Kamihara,[51,61] J. Kamin,[58] M. Kaneta,[52] J. H. Kang,[67] H. Kanou,[51,61] T. Kawagishi,[62] D. Kawall,[52] A. V. Kazantsev,[31] S. Kelly,[11] A. Khanzadeev,[50] J. Kikuchi,[64] D. H. Kim,[41] D. J. Kim,[67] E. Kim,[56] Y.-S. Kim,[28] E. Kinney,[11] Á. Kiss,[16] E. Kistenev,[6] A. Kiyomichi,[51] J. Klay,[35] C. Klein-Boesing,[40] L. Kochenda,[50] V. Kochetkov,[21] B. Komkov,[50] M. Konno,[62] D. Kotchetkov,[7] A. Kozlov,[65] A. Král,[13] A. Kravitz,[12] P. J. Kroon,[6] J. Kubart,[8,24] G. J. Kunde,[36] N. Kurihara,[10] K. Kurita,[51,53] M. J. Kweon,[30] Y. Kwon,[60,67] G. S. Kyle,[45] R. Lacey,[57] Y. S. Lai,[12] J. G. Lajoie,[25] A. Lebedev,[25] Y. Le Bornec,[48] S. Leckey,[58] D. M. Lee,[36] M. K. Lee,[67] T. Lee,[56] M. J. Leitch,[36] M. A. L. Leite,[55] B. Lenzi,[55] X. Li,[9] X. H. Li,[7] H. Lim,[56] T. Liška,[13] A. Litvinenko,[27] M. X. Liu,[36] B. Love,[63] D. Lynch,[6] C. F. Maguire,[63] Y. I. Makdisi,[5,6] A. Malakhov,[27] M. D. Malik,[44] V. I. Manko,[31] Y. Mao,[49,51] L. Mašek,[8,24] H. Masui,[62] F. Matathias,[12,58] M. C. McCain,[22] M. McCumber,[58] P. L. McGaughey,[36] Y. Miake,[62] P. Mikeš,[8,24] K. Miki,[62] T. E. Miller,[63] A. Milov,[58] S. Mioduszewski,[6] G. C. Mishra,[19] M. Mishra,[3] J. T. Mitchell,[6] M. Mitrovski,[57] A. Morreale,[7] D. P. Morrison,[6,†] J. M. Moss,[36] T. V. Moukhanova,[31] D. Mukhopadhyay,[63] J. Murata,[51,53] S. Nagamiya,[29,51] Y. Nagata,[62] J. L. Nagle,[11,‡] M. Naglis,[65] I. Nakagawa,[51,52] Y. Nakamiya,[20] T. Nakamura,[20] K. Nakano,[51,61] J. Newby,[35] M. Nguyen,[58] B. E. Norman,[36] R. Nouicer,[6] A. S. Nyanin,[31] J. Nystrand,[38] E. O'Brien,[6] S. X. Oda,[10] C. A. Ogilvie,[25] H. Ohnishi,[51] I. D. Ojha,[63] M. Oka,[62] K. Okada,[52] O. O. Omiwade,[1] A. Oskarsson,[38] I. Otterlund,[38] M. Ouchida,[20] K. Ozawa,[10] R. Pak,[6] D. Pal,[63] A. P. T. Palounek,[36] V. Pantuev,[23,58] V. Papavassiliou,[45] J. Park,[56] W. J. Park,[30] S. F. Pate,[45] H. Pei,[25] J.-C. Peng,[22] H. Pereira,[14] V. Peresedov,[27] D. Yu. Peressounko,[31] C. Pinkenburg,[6] R. P. Pisani,[6] M. L. Purschke,[6] A. K. Purwar,[36,58] H. Qu,[19] J. Rak,[25,44] A. Rakotozafindrabe,[33] I. Ravinovich,[65] K. F. Read,[47,60] S. Rembeczki,[17] M. Reuter,[58] K. Reygers,[40] V. Riabov,[43,50] Y. Riabov,[50] G. Roche,[37] A. Romana,[33,*] M. Rosati,[25] S. S. E. Rosendahl,[38] P. Rosnet,[37] P. Rukoyatkin,[27] V. L. Rykov,[51] S. S. Ryu,[67] B. Sahlmueller,[40,58] N. Saito,[32,51,52] T. Sakaguchi,[6,10,64] S. Sakai,[62] H. Sakata,[20] V. Samsonov,[43,50] H. D. Sato,[32,51] S. Sato,[6,26,29] S. Sawada,[29] J. Seele,[11] R. Seidl,[22] V. Semenov,[21] R. Seto,[7] D. Sharma,[65] T. K. Shea,[6] I. Shein,[21] A. Shevel,[50,57] T.-A. Shibata,[51,61] K. Shigaki,[20] M. Shimomura,[62] T. Shohjoh,[62] K. Shoji,[32,51] A. Sickles,[22,58] C. L. Silva,[55] D. Silvermyr,[47] C. Silvestre,[14] K. S. Sim,[30] C. P. Singh,[3] V. Singh,[3] S. Skutnik,[25] M. Slunečka,[8,27] W. C. Smith,[1] A. Soldatov,[21] R. A. Soltz,[35] W. E. Sondheim,[36] S. P. Sorensen,[60] I. V. Sourikova,[6] F. Staley,[14] P. W. Stankus,[47] E. Stenlund,[38] M. Stepanov,[45,*] A. Ster,[66] S. P. Stoll,[6] T. Sugitate,[20] C. Suire,[48] J. P. Sullivan,[36] J. Sziklai,[66] T. Tabaru,[52] S. Takagi,[62] E. M. Takagui,[55] A. Taketani,[51,52] K. H. Tanaka,[29] Y. Tanaka,[42] K. Tanida,[51,52,56] M. J. Tannenbaum,[6] A. Taranenko,[43,57] P. Tarján,[15] T. L. Thomas,[44] T. Todoroki,[51,62] M. Togawa,[32,51] A. Toia,[58] J. Tojo,[51] L. Tomášek,[24] H. Torii,[51] R. S. Towell,[1] V-N. Tram,[33] I. Tserruya,[65] Y. Tsuchimoto,[20,51] S. K. Tuli,[3,*] H. Tydesjö,[38] N. Tyurin,[21] C. Vale,[25] H. Valle,[63] H. W. van Hecke,[36] J. Velkovska,[63] R. Vértesi,[15] A. A. Vinogradov,[31] M. Virius,[13] V. Vrba,[24] E. Vznuzdaev,[50] M. Wagner,[32,51] D. Walker,[58] X. R. Wang,[45] Y. Watanabe,[51,52] J. Wessels,[40] S. N. White,[6] N. Willis,[48] D. Winter,[12] C. L. Woody,[6] M. Wysocki,[11] W. Xie,[7,52] Y. L. Yamaguchi,[64] A. Yanovich,[21] Z. Yasin,[7] J. Ying,[19] S. Yokkaichi,[51,52] G. R. Young,[47] I. Younus,[34,44] I. E. Yushmanov,[31] W. A. Zajc,[12] O. Zaudtke,[40] C. Zhang,[12,47] S. Zhou,[9] J. Zimányi,[66,*] and L. Zolin[27]

(PHENIX Collaboration)

[1]*Abilene Christian University, Abilene, Texas 79699, USA*

[2]*Department of Physics, Augustana University, Sioux Falls, South Dakota 57197, USA*

[3]*Department of Physics, Banaras Hindu University, Varanasi 221005, India*
[4]*Baruch College, City University of New York, New York, New York 10010, USA*
[5]*Collider-Accelerator Department, Brookhaven National Laboratory, Upton, New York 11973-5000, USA*
[6]*Physics Department, Brookhaven National Laboratory, Upton, New York 11973-5000, USA*
[7]*University of California-Riverside, Riverside, California 92521, USA*
[8]*Charles University, Ovocný trh 5, Praha 1, 116 36 Prague, Czech Republic*
[9]*Science and Technology on Nuclear Data Laboratory, China Institute of Atomic Energy, Beijing 102413, People's Republic of China*
[10]*Center for Nuclear Study, Graduate School of Science, University of Tokyo, 7-3-1 Hongo, Bunkyo, Tokyo 113-0033, Japan*
[11]*University of Colorado, Boulder, Colorado 80309, USA*
[12]*Columbia University, New York, New York 10027, USA and Nevis Laboratories, Irvington, New York 10533, USA*
[13]*Czech Technical University, Zikova 4, 166 36 Prague 6, Czech Republic*
[14]*Dapnia, CEA Saclay, F-91191 Gif-sur-Yvette, France*
[15]*Debrecen University, H-4010 Debrecen, Egyetem tér 1, Hungary*
[16]*ELTE, Eötvös Loránd University, H-1117 Budapest, Pázmany Péter sétány 1/A, Hungary*
[17]*Florida Institute of Technology, Melbourne, Florida 32901, USA*
[18]*Florida State University, Tallahassee, Florida 32306, USA*
[19]*Georgia State University, Atlanta, Georgia 30303, USA*
[20]*Hiroshima University, Kagamiyama, Higashi-Hiroshima 739-8526, Japan*
[21]*IHEP Protvino, State Research Center of Russian Federation, Institute for High Energy Physics, Protvino 142281, Russia*
[22]*University of Illinois at Urbana-Champaign, Urbana, Illinois 61801, USA*
[23]*Institute for Nuclear Research of the Russian Academy of Sciences, prospekt 60-letiya Oktyabrya 7a, Moscow 117312, Russia*
[24]*Institute of Physics, Academy of Sciences of the Czech Republic, Na Slovance 2, 182 21 Prague 8, Czech Republic*
[25]*Iowa State University, Ames, Iowa 50011, USA*
[26]*Advanced Science Research Center, Japan Atomic Energy Agency, 2-4 Shirakata Shirane, Tokai-mura, Naka-gun, Ibaraki-ken 319-1195, Japan*
[27]*Joint Institute for Nuclear Research, 141980 Dubna, Moscow Region, Russia*
[28]*KAERI, Cyclotron Application Laboratory, Seoul, Korea*
[29]*KEK, High Energy Accelerator Research Organization, Tsukuba, Ibaraki 305-0801, Japan*
[30]*Korea University, Seoul 136-701, Korea*
[31]*Russian Research Center "Kurchatov Institute," Moscow 123098, Russia*
[32]*Kyoto University, Kyoto 606-8502, Japan*
[33]*Laboratoire Leprince-Ringuet, Ecole Polytechnique, CNRS-IN2P3, Route de Saclay, F-91128 Palaiseau, France*
[34]*Physics Department, Lahore University of Management Sciences, Lahore 54792, Pakistan*
[35]*Lawrence Livermore National Laboratory, Livermore, California 94550, USA*
[36]*Los Alamos National Laboratory, Los Alamos, New Mexico 87545, USA*
[37]*LPC, Université Blaise Pascal, CNRS-IN2P3, Clermont-Fd, 63177 Aubiere Cedex, France*
[38]*Department of Physics, Lund University, Box 118, SE-221 00 Lund, Sweden*
[39]*Department of Physics, University of Michigan, Ann Arbor, Michigan 48109-1040, USA*
[40]*Institut für Kernphysik, University of Muenster, D-48149 Muenster, Germany*
[41]*Myongji University, Yongin, Kyonggido 449-728, Korea*
[42]*Nagasaki Institute of Applied Science, Nagasaki-shi, Nagasaki 851-0193, Japan*
[43]*National Research Nuclear University, MEPhI, Moscow Engineering Physics Institute, Moscow 115409, Russia*
[44]*University of New Mexico, Albuquerque, New Mexico 87131, USA*
[45]*New Mexico State University, Las Cruces, New Mexico 88003, USA*
[46]*Department of Physics and Astronomy, Ohio University, Athens, Ohio 45701, USA*
[47]*Oak Ridge National Laboratory, Oak Ridge, Tennessee 37831, USA*
[48]*IPN-Orsay, Universite Paris Sud, CNRS-IN2P3, BP1, F-91406 Orsay, France*
[49]*Peking University, Beijing 100871, People's Republic of China*
[50]*PNPI, Petersburg Nuclear Physics Institute, Gatchina, Leningrad Region 188300, Russia*
[51]*RIKEN Nishina Center for Accelerator-Based Science, Wako, Saitama 351-0198, Japan*
[52]*RIKEN BNL Research Center, Brookhaven National Laboratory, Upton, New York 11973-5000, USA*
[53]*Physics Department, Rikkyo University, 3-34-1 Nishi-Ikebukuro, Toshima, Tokyo 171-8501, Japan*
[54]*Saint Petersburg State Polytechnic University, St. Petersburg 195251, Russia*
[55]*Universidade de São Paulo, Instituto de Física, Caixa Postal 66318, São Paulo CEP05315-970, Brazil*
[56]*Department of Physics and Astronomy, Seoul National University, Seoul 151-742, Korea*
[57]*Chemistry Department, Stony Brook University, SUNY, Stony Brook, New York 11794-3400, USA*
[58]*Department of Physics and Astronomy, Stony Brook University, SUNY, Stony Brook, New York 11794-3800, USA*
[59]*SUBATECH (Ecole des Mines de Nantes, CNRS-IN2P3, Université de Nantes) BP 20722-44307, Nantes, France*
[60]*University of Tennessee, Knoxville, Tennessee 37996, USA*

[61]*Department of Physics, Tokyo Institute of Technology, Oh-okayama, Meguro, Tokyo 152-8551, Japan*
[62]*Center for Integrated Research in Fundamental Science and Engineering, University of Tsukuba, Tsukuba, Ibaraki 305, Japan*
[63]*Vanderbilt University, Nashville, Tennessee 37235, USA*
[64]*Waseda University, Advanced Research Institute for Science and Engineering, 17 Kikui-cho, Shinjuku-ku, Tokyo 162-0044, Japan*
[65]*Weizmann Institute, Rehovot 76100, Israel*
[66]*Institute for Particle and Nuclear Physics, Wigner Research Centre for Physics, Hungarian Academy of Sciences (Wigner RCP, RMKI), Budapest 114, P.O. Box 49, H-1525 Budapest, Hungary*
[67]*Yonsei University, IPAP, Seoul 120-749, Korea*

(Received 3 December 2014; published 23 September 2015)

We have studied the dependence of azimuthal anisotropy v_2 for inclusive and identified charged hadrons in Au + Au and Cu + Cu collisions on collision energy, species, and centrality. The values of v_2 as a function of transverse momentum p_T and centrality in Au + Au collisions at $\sqrt{s_{_{NN}}} = 200$ and 62.4 GeV are the same within uncertainties. However, in Cu + Cu collisions we observe a decrease in v_2 values as the collision energy is reduced from 200 to 62.4 GeV. The decrease is larger in the more peripheral collisions. By examining both Au + Au and Cu + Cu collisions we find that v_2 depends both on eccentricity and the number of participants, $N_{\rm part}$. We observe that v_2 divided by eccentricity (ε) monotonically increases with $N_{\rm part}$ and scales as $N_{\rm part}^{1/3}$. The Cu + Cu data at 62.4 GeV falls below the other scaled v_2 data. For identified hadrons, v_2 divided by the number of constituent quarks n_q is independent of hadron species as a function of transverse kinetic energy $KE_T = m_T - m$ between $0.1 < KE_T/n_q < 1$ GeV. Combining all of the above scaling and normalizations, we observe a near-universal scaling, with the exception of the Cu + Cu data at 62.4 GeV, of $v_2/(n_q \cdot \varepsilon \cdot N_{\rm part}^{1/3})$ vs KE_T/n_q for all measured particles.

DOI: 10.1103/PhysRevC.92.034913 PACS number(s): 25.75.Dw

I. INTRODUCTION

The azimuthal anisotropy of particles produced in relativistic heavy-ion collisions is a powerful probe for investigating the characteristics of the quark-gluon plasma (QGP) [1–4]. The elliptic azimuthal anisotropy (v_2) is defined by the amplitude of the second-order harmonic in a Fourier series expansion of emitted particle azimuthal distributions,

$$v_2 = \langle \cos(2[\phi - \Psi_{\rm RP}]) \rangle, \qquad (1)$$

where ϕ represents the azimuthal emission angle of a particle and $\Psi_{\rm RP}$ is the azimuthal angle of the reaction plane (RP), which is defined by the impact parameter and the beam axis. The brackets denote statistical averaging over particles and events. Elliptic flow is sensitive to the early stage of heavy-ion collisions because pressure gradients transfer the initial geometrical anisotropy of the collision region to an anisotropy in momentum space.

One of the most remarkable findings at the Relativistic Heavy Ion Collider (RHIC) is that the strength of v_2 [5] is much larger than what is expected from a hadronic scenario [6]. Moreover, a scaling of v_2 by the number of constituent quarks in a hadron in the intermediate transverse momentum region ($p_T = 1$–4 GeV/c) has been found for a broad range of particle species produced in Au + Au at $\sqrt{s_{_{NN}}} = 200$ GeV [7,8]. Both STAR and PHENIX experiments have observed that v_2 scales better as a function of the transverse kinetic energy of the hadron. These scalings of v_2 are consistent with constituent quark flow at early collision times and recombination as the dominant process of hadronization.

The detailed interpretation of v_2 results requires modeling [9,10] of the wave function of the incoming nuclei, fluctuations of the initial geometry, viscous relativistic hydrodynamics, hadronic freeze-out, and subsequent rescattering, along with various model parameters such as the assumed equation of state and transport coefficients, e.g., viscosity. In recent calculations, the strength of v_2 for hadrons in heavy-ion collisions at $\sqrt{s_{_{NN}}} = 200$ GeV can be reproduced by hydrodynamical models that include shear viscosity and initial fluctuations [11–13].

At the LHC, experiments have measured v_2 as a function of p_T from Pb + Pb collisions at an order of magnitude higher beam energy, at $\sqrt{s_{_{NN}}} = 2.76$ TeV [14–16]. These v_2 results as a function of p_T for inclusive hadrons are very similar in magnitude and shape to the RHIC measurements at 200 GeV. However, the v_2 measurements for identified hadrons at LHC [17,18] below 3 GeV/c do not scale well with the quark number and transverse kinetic energy of the hadron with deviations up to 40%.

A comparison of measured v_2 at the lower beam energies at RHIC ($\sqrt{s_{_{NN}}} = 7.7$–200 GeV) shows that v_2 as a function of p_T seems to be saturated above $\sqrt{s_{_{NN}}} = 39$ GeV and decreases below this beam energy [19]. The scaling of v_2 with transverse kinetic energy is broken below a beam energy of 19 GeV [19]. Possible explanations for this behavior include rescattering in the later hadronic phase, incomplete thermalization in the initial stage, or the plasma not being formed at these lower beam energies.

Because transverse kinetic energy scaling is broken at energies significantly lower and higher than RHIC's full energy of 200 GeV, it is important to provide systematic measurements

---

[*] Deceased.

[†] PHENIX Cospokesperson: morrison@bnl.gov

[‡] PHENIX Cospokesperson: jamie.nagle@colorado.edu

of v_2 for identified hadrons as a function of system size, collision energy, and centrality. These systematics are needed to make progress on the nature of the QGP at lower energy density. We report on such a set of measurements in this paper, examining both Au + Au and Cu + Cu collisions at 200- and 62.4-GeV beam energies. This adds to the low-energy Au + Au measurements made by STAR [19] and their Cu + Cu v_2 data at 200- and 62.4-GeV beam energies [20]. The system size dependence of flow is particularly important because long-range azimuthal correlations have also been observed in high-multiplicity events from much smaller systems such as d + Au collisions [21] at RHIC, $p + p$ [22], and p + Pb collisions [23] at LHC. The origin of these anisotropies is currently unknown; various competing explanations include parton saturation and hydrodynamic flow.

We expect that the systematic study of v_2 for inclusive and identified particles can provide information on the temperature dependence of η/s (i.e., the ratio of shear viscosity to entropy density s), the impact of viscosity on systems of different sizes, as well as constraining models of the reaction dynamics.

The organization of this paper is as follows. Section II describes the PHENIX detector used for this analysis, Sec. III describes the experimental method of azimuthal anisotropy analysis, Sec. IV presents the results of the systematic study for inclusive charged hadron v_2, and Sec. V presents the results of the systematic study for the v_2 of identified charged hadrons. The new data published in this paper are the Cu + Cu data at 62.4 GeV, as well the Au + Au v_2 results for $p_T > 5$ GeV/c. Other data come from prior PHENIX publications [7,24].

II. PHENIX DETECTOR

The results that we present in this paper were obtained with the PHENIX detector at RHIC [25]. We discuss below the main detector components that were used for this analysis.

A. Global detectors

The beam-beam counters (BBCs) are located 144 cm upstream and downstream of the beam crossing point. Each BBC comprises 64 individual quartz Čerenkov counters and covers the full azimuthal angle in the pseudorapidity range $3.0 < |\eta| < 3.9$. The average of the times measured by the two BBCs from fast leading particles provide the start time for the event, while the difference in times provides the vertex position of the collision. The timing and position resolution of the BBCs are 20 ps and 0.6 cm, respectively, for both Au + Au and Cu + Cu collisions. The event start time is also used for particle identification (PID) through the time-of-flight to the TOF and EMCal subsystems in the PHENIX central arms.

The zero-degree calorimeters (ZDCs) cover the pseudorapidity range $|\eta| > 6$ and measure the energy of spectator neutrons with an energy resolution of approximately 20%. More details about these detectors can be found in Ref. [26].

B. Central-arm tracking detectors

Two (identical) drift chambers (DCs) are installed in the East and West arms of the PHENIX central detector and are located between 2.02 and 2.46 m radial distance from the interaction point. Each of the two DCs extends 180 cm along the beam direction and subtends $\pi/2$ in azimuth. The momentum resolution for tracks reconstructed by the DC is $0.7\% \oplus 1.1\% p$ (GeV/c). The position of the DCs relative to the other detectors in the central spectrometer is shown in Fig. 1 and details of the DC construction and tracking performance can be found in Ref. [27].

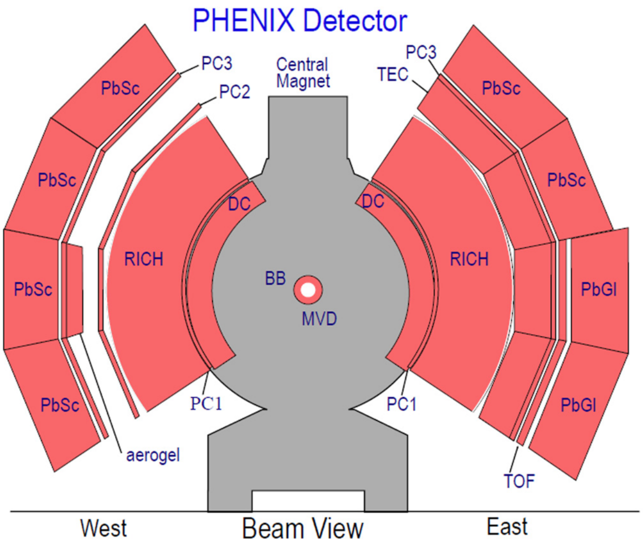

FIG. 1. (Color online) Installed and active detectors for the RUN-4 configuration of the PHENIX experiment. Shown are the two central spectrometer arms viewed in a cut through the collision vertex.

The PHENIX pad chambers (PCs) are multiwire proportional chambers composed of three separate layers of pixel detectors. Each PC detector contains a single plane of wires in a gas volume bounded by two cathode planes. The innermost PC plane, PC1, is located between the DC and a ring-imaging Čerenkov counter (RICH) on both the East and the West arms, PC2 is placed in back of the RICH on the West arm only, and PC3 is located in front of the electromagnetic calorimeters on both the East and the West arms.

The PC system determines space points outside the magnetic field and hence provides straight-line particle trajectories. They are the only nonprojective detectors in the central tracking system and thus are critical elements of the pattern recognition. PC1 is also essential for determining the three-dimensional momentum vector by providing the z coordinate of each track at the exit of the DC. Details of the PC construction and their performance can be found in Ref. [27].

C. Time-of-flight counters

The PHENIX time-of-flight (TOF) detector serves as a PID device for charged hadrons. The time resolution for the BBC-TOF system is around 120 ps, which enables 2σ separation of π/K up to 2.0 GeV/c. The length of the flight path of each track from the event vertex to the TOF detector is calculated by the momentum reconstruction algorithm. The length and TOF are combined to identify the charged particles. The TOF is located between the PC3 and EMCal in the East arm and about 5.06 m away from the collision vertex. It covers $|\eta| < 0.35$ and

TABLE I. Information on the data sets and event statistics.

Year	Species	Energy (GeV)	No. of events
2004	Au + Au	200	8.2×10^8
2004	Au + Au	62.4	2.6×10^7
2005	Cu + Cu	200	8.0×10^8
2005	Cu + Cu	62.4	3.4×10^8

azimuthal angle $\Delta\phi = 45^\circ$. Details of the TOF construction and performance can be found in Ref. [26].

D. Electromagnetic calorimeter

The PHENIX EMCal was designed to measure the spatial position and energy of electrons and photons produced in heavy-ion collisions. The EMCal covers the full central spectrometer acceptance of $|\eta| < 0.35$ and is installed in both arms, each subtending 90° in azimuth, i.e., larger than the TOF acceptance. The EMCal comprises six sectors of lead-scintillator (PbSc) calorimeters and two sectors of lead-glass (PbGl) calorimeters. The PbGl is not used in this analysis, but we note that the TOF detector is in front of the PbGl, so no PID coverage is lost. The PbSc is a sampling calorimeter and has a timing resolution of 400 ps for hadrons. The PbSc can be used to separate π/K with 2σ up to 1.0 GeV/c. Details of the PbSc construction and performance are described in Ref. [28].

E. RICH

A ring-imaging Čerenkov counter (RICH) is installed on each of the PHENIX central arms. Each RICH detector is a threshold gas Čerenkov detector with a high angular segmentation filled with CO_2 gas. In this analysis we use the RICH to reject electrons by removing tracks that match to a RICH ring. It is noted that charged pions with p_T larger than 4 GeV/c also radiate in the CO_2 gas.

III. EXPERIMENTAL METHOD

A. Data sets and event selection

We measured Cu + Cu and Au + Au collisions at $\sqrt{s_{_{NN}}} =$ 62.4 and 200 GeV. The Cu + Cu data were taken during RHIC Run-5 (2005) and Au + Au data were taken during RHIC Run-4 (2004) running periods. We used a minimum bias trigger that was defined by a coincidence between the two BBCs and an energy threshold of one neutron in both ZDCs. The collision vertex along the beam direction, z, was measured by the BBC. The total number of minimum bias events that were analyzed after requiring an off-line vertex cut of $|z| < 30$ cm and selecting good runs are listed in Table I.

In Au + Au collisions at 200 GeV the centrality of the collision was determined by using the correlation of the total energy deposited in the ZDCs with the total charge deposited in the BBCs, as described in Ref. [29]. However, in 200-GeV Cu + Cu, 62.4-GeV Cu + Cu, and 62.4-GeV Au + Au collisions, the resolving power of the ZDCs is insufficient to significantly contribute to the centrality definition. Therefore, the total charge deposited in the BBCs is used to determine centrality in these collision systems, as described in Ref. [29]. A Glauber-model Monte-Carlo simulation of the each collision [30,31] was used to estimate the average number of participating nucleons $N_{\rm part}$ and participant eccentricity (ε), which includes the effect of fluctuations from the initial participant geometry. This simulation includes modeling of the BBC and ZDC response. Table II summarizes $N_{\rm part}$, its systematic uncertainties ($\Delta N_{\rm part}$), ε, and its systematic uncertainties ($\Delta\varepsilon$).

B. Track selection

The analysis was performed for inclusive charged hadrons over the transverse momentum range $0.2 < p_T < 10$ GeV/c and for identified charged particles [pions ($\pi^+ + \pi^-$), kaons ($K^+ + K^-$), and protons ($p + \bar{p}$)] in the momentum range up to p_T 2.2, 3, and 4 GeV/c, respectively.

The track reconstruction procedure is described in Ref. [32]. Tracks reconstructed by the DC that do not originate from the event vertex have been investigated as background to the inclusive charged-particle measurement. The main background sources include secondary particles from hadron decays and e^+e^- pairs from the conversion of photons in the material between the vertex and the DC [33]. To minimize background originating from the magnets, reconstructed tracks are required to have a z position less than ±80 cm when the tracks cross the outer radius of the DC. The DC is outside the central magnet

TABLE II. Number of participants ($N_{\rm part}$), its uncertainty ($\Delta N_{\rm part}$), participant eccentricity (ε), and its uncertainty ($\Delta\varepsilon$) from Glauber Monte Carlo calculations for Au + Au and Cu + Cu collisions at 200 and 62.4 GeV.

Centrality bin (%)	Au + Au 200 GeV				Au + Au 62.4 GeV				Cu + Cu 200 GeV				Cu + Cu 62.4 GeV			
	$N_{\rm part}$	$\Delta N_{\rm part}$	ε	$\Delta\varepsilon$ (%)	$N_{\rm part}$	$\Delta N_{\rm part}$	ε	$\Delta\varepsilon$ (%)	$N_{\rm part}$	$\Delta N_{\rm part}$	ε	$\Delta\varepsilon$ (%)	$N_{\rm part}$	$\Delta N_{\rm part}$	ε	$\Delta\varepsilon$ (%)
0–10	325.2	3.3	0.103	2.6	320.7	7.9	0.107	2.3	98.2	2.4	0.163	2.0	93.3	2.6	0.169	1.7
10–20	234.6	4.7	0.200	2.5	230.7	9.2	0.207	2.2	73.6	2.5	0.241	3.0	71.1	2.4	0.248	2.6
20–30	166.6	5.4	0.284	2.1	163.2	7.6	0.292	2.0	53.0	1.9	0.317	1.9	51.3	2.0	0.324	1.9
30–40	114.2	4.4	0.356	1.7	113.0	5.6	0.365	1.8	37.3	1.6	0.401	1.9	36.2	1.8	0.408	1.6
40–50	74.4	3.8	0.422	1.5	74.5	4.1	0.431	1.3	25.4	1.3	0.484	1.6	24.9	1.5	0.494	2.1
50–60	45.5	3.3	0.491	1.1	45.9	3.1	0.498	1.0	16.7	0.9	0.579	1.4	16.1	0.9	0.587	1.5
60–70	25.7	3.8	0.567	0.7	25.9	1.7	0.573	0.8	10.4	0.6	0.674	2.1			0.696	2.3
70–80	13.4	3.0	0.666	1.2			0.678	1.1	6.4	0.5	0.721	1.7			0.742	1.6
80–90			0.726	2.8			0.740	2.2			0.856	7.2			0.867	6.2

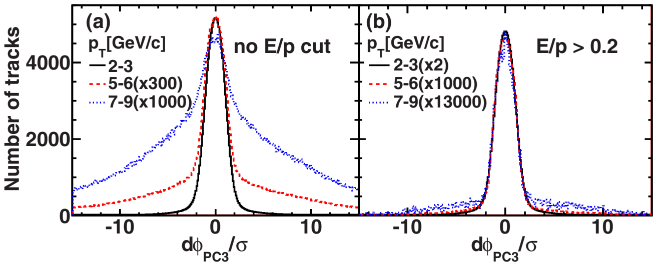

FIG. 2. (Color online) (a) Track/hit matching distribution of $d\phi/\sigma$ at PC3 without E/p cut for indicated p_T bins; (b) same quantity, but after applying an $E/p > 0.2$ cut.

field; hence, we can approximate reconstructed tracks through the central-arm detectors as straight lines. This enables tracks to be projected to outer detectors and matched to measured hits. Good tracks are required to be matched to a hit in the PC3, as well as in the EMCal, within 2.5σ of the expected hit location in both azimuthal and beam directions.

The RICH also reduces the conversion background. For tracks with $p_T < 4$ GeV/c we apply a cut of $n_0 < 0$, where n_0 is the number of fired phototubes in the RICH ring. For $p_T > 4$ GeV/c, we require tracks to have $E/p > 0.2$, where E denotes the energy deposited in the EMCal and p_T is the transverse momentum of particles measured in the DC. Because most of the background from photon conversion are low-momentum particles that were incorrectly reconstructed at higher momentum, when we require a large deposit of energy in the EMCal, this suppresses the conversion background [34].

To demonstrate the effectiveness of the E/p cut, Fig. 2 shows the track/hit matching distributions $d\phi/\sigma$ at PC3, where $d\phi$ is the residual between the track projection point and the detector hit position along ϕ and σ is the standard deviation of the $d\phi$ distribution. The left panel shows the $d\phi/\sigma$ without an E/p cut, and the right panel shows the distribution with a cut of $E/p > 0.2$. Note that the vertical scale between the panels is different. The $E/p > 0.2$ cut substantially reduces the background for high-p_T tracks. The residual background remaining after these cuts has been estimated by the fitting the $d\phi/\sigma$ distributions in PC3 with a double Gaussian function (signal and background). The signal and residual background distributions are required to have the same mean. For $p_T <$ 4 GeV/c the residual background is less than 5% of the real tracks and reaches 10% for p_T 8–10 GeV/c. The efficiency of the $E/p > 0.2$ cut is 0.3 at $p_T = 5$–6 GeV/c and 0.1 at $p_T = 7$–9 GeV/c.

C. Particle identification

For identified charged hadrons we also require the tracks to have a hit in the TOF detector or EMCal within, at most, 2σ of the expected hit location in both azimuthal and beam directions. Particles are identified by their mass squared, using the momentum measurement from the DC (p), TOF between BBC and TOF/EMCal (t), and flight-path length (L) from the collision vertex point to the hit position on the TOF wall or cluster in the EMCal. The square of the particle's mass is calculated as

$$m^2 = \frac{p^2}{c^2}\left[\left(\frac{t}{L/c}\right)^2 - 1\right]. \tag{2}$$

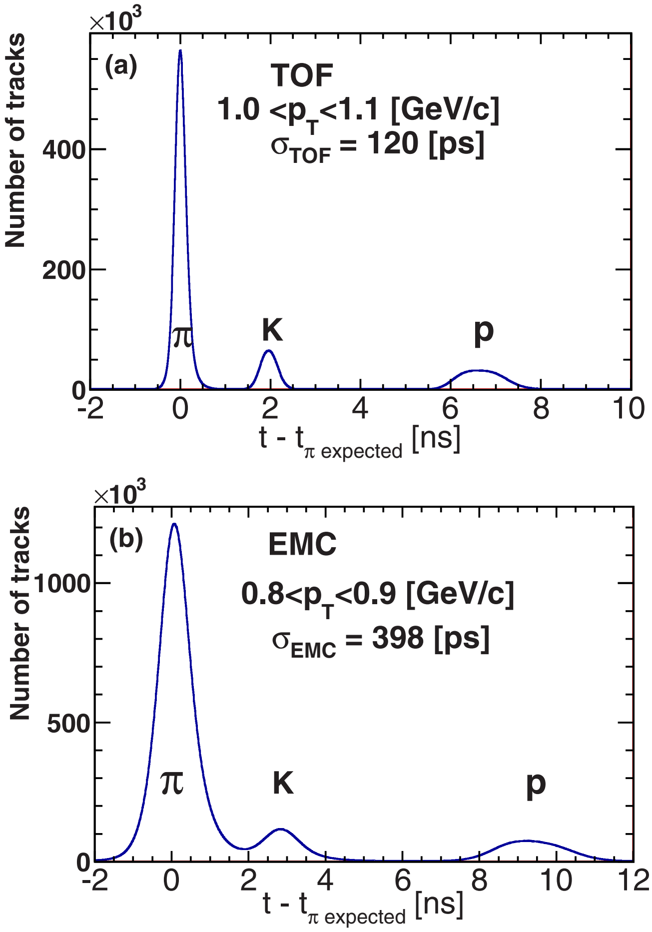

FIG. 3. (Color online) Distributions of $t - t_{\pi\text{expected}}$, the difference between the measured TOF in the TOF (upper) and EMC (lower) and the time calculated assuming each candidate track is a pion. Resolutions are $\sigma_T \sim 120$ ps for TOF and $\sigma_T \sim 400$ ps for EMCal in Au + Au at 200-GeV data.

The timing resolution of the BBC-TOF and BBC-EMCal systems was determined by examining the timing difference between the measured flight time t and $t_{\pi\text{expected}}$, the time which is expected under the assumption that the particles are pions. The resulting time distribution is shown in Fig. 3. A narrow peak centered around $t - t_{\pi\text{expected}} \approx 0$ corresponds to pions, and the other two broad peaks are kaons and protons. A Gaussian distribution is fit to the pion peak and yields a resolution of ~120 ps for the BBC-TOF system and ~400 ps for the BBC-EMCal system.

The PID is performed by applying momentum-dependent cuts in mass squared (m^2). The m^2 distributions are fit with a 3-G function corresponding to pions, kaons, and protons. The corresponding widths and centroids are extracted from the data as a function of transverse momentum. To select candidate tracks of a particle species, the m^2 is required to be within 2σ for the selected particles species and outside 2.5σ for the other particle species. This provides a sample for each particle species with at least 90% purity in PID. For the BBC-TOF system the upper momentum cutoff is 2.2 GeV/c for kaons and 3 GeV/c for pions. For protons the upper momentum cutoff is 4 GeV/c. For the BBC-EMCal system the upper momentum cutoff is 1 GeV/c for kaons and 1.4 GeV/c for pions. For protons the upper momentum cutoff is 2.2 GeV/c. The lower momentum cutoff for both PID systems is 0.2 GeV/c for pions, 0.3 GeV/c for kaons, and 0.5 GeV/c for protons. The PID results for the 200-GeV Au + Au data set were obtained using TOF detector only; for the 62.4-GeV Au + Au and 200-GeV Cu + Cu data sets the PID results were obtained by including identified particles from either the TOF or EMCal over different momentum ranges. For overlap region, we use BBC-EMC because of the better statistics and include the differences between BBC-EMC and BBC-TOF as systematic uncertainty shown in Table VI. No correction is applied for any contamination from misidentified hadrons.

D. Azimuthal anisotropy: Event-plane method

Because the principal axis of the participants cannot be measured directly in the experiment, the azimuthal angle of the reaction plane is estimated [35]. The estimated reaction plane is called the "event plane" and is determined for each harmonic of the Fourier expansion of the azimuthal distribution. The event-flow vector $\vec{Q}_n = (Q_x, Q_y)$ and azimuth of the event plane Ψ_n for nth harmonic of the azimuthal anisotropy can be expressed as

$$Q_x \equiv |\vec{Q}_n|\cos(n\Psi_n) = \sum_i^M w_i \cos(n\phi_i), \tag{3}$$

$$Q_y \equiv |\vec{Q}_n|\sin(n\Psi_n) = \sum_i^M w_i \sin(n\phi_i), \tag{4}$$

$$\Psi_n = \frac{1}{n}\tan^{-1}\left(\frac{Q_y}{Q_x}\right), \tag{5}$$

where M denotes the number of particles used to determine the event plane, ϕ_i is the azimuthal angle of each particle, and the weight w_i is the charge seen in the corresponding channel of the BBC. Once the event plane is determined, the elliptic flow v_2 can be extracted by correlating the azimuthal angle of emitted particles ϕ with the event plane,

$$v_2\{\Psi n\} = \frac{v_2{}^{\rm obs}}{{\rm Res}\{\Psi_n\}} = \frac{\langle\cos(2[\phi - \Psi_n])\rangle}{\langle\cos(2[\Psi_n - \Psi_{\rm RP}])\rangle}, \tag{6}$$

where ϕ is the azimuthal angle of tracks in the laboratory frame, Ψ_n is the nth-order event plane and the brackets denote an average over all charged tracks and events. The denominator Res$\{\Psi_n\}$ is the event-plane resolution that corrects for the difference between the estimated event plane Ψ_n and true reaction plane $\Psi_{\rm RP}$. We measure v_2 using the same harmonic event plane (Ψ_2) because this leads to a better accuracy [35].

The second-harmonic event planes were independently determined with two BBCs located at forward (BBC South) and backward (BBC North) pseudorapidities $|\eta| = 3.1$–3.9 [5]. The planes were also combined to provide the event plane for the full event. More details on using the BBC for the reaction-plane measurement can be found in Ref. [24]. The measured v_2 of hadrons in the central arms with respect to the combined second-harmonic BBC event plane are denoted throughout this paper as v_2.

1. Event-plane determination

To determine each event plane, we chose the weights at each azimuthal angle to be the charge seen in the corresponding channel of the BBC. Corrections were performed to remove possible biases from small nonuniformities in the acceptance of the BBC. In this analysis we applied two corrections: the recentering and shift methods [35]. In the recentering method, event-flow vectors are shifted and normalized using the mean $\langle Q\rangle$ and width σ of the Q vector distribution:

$$Q'_x = \frac{Q_x - \langle Q_x\rangle}{\sigma_x}, \quad Q'_y = \frac{Q_y - \langle Q_y\rangle}{\sigma_y}. \tag{7}$$

This correction reduces the dependence of the event-plane resolution on the laboratory angle. Most acceptance effects are removed by this recentering method. The shift method was used as a final correction [35]. In the shift method the reaction plane is shifted by $\Delta\Psi_n$ defined by

$$n\Delta\Psi_n(\Psi_n) = \sum_{k=1}^{k_{\rm max}} \frac{2}{k}[-\langle\sin(kn\Psi_n)\rangle\cos(kn\Psi_n) + \langle\cos(kn\Psi_n)\rangle\sin(kn\Psi_n)], \tag{8}$$

where $k_{\rm max} = 8$ in this analysis. The shift ensures that $dN/d\Psi_n$ is isotropic. When $k_{\rm max}$ was reduced to $k_{\rm max} = 4$, the difference in the extracted v_2 was negligible and thus we include no systematic uncertainty owing to the choice of $k_{\rm max}$ in our v_2 results [24].

Independent recentering and shift corrections were applied to each centrality selection, in 5% increments, as well as 20-cm steps in the z vertex. This optimizes the event-plane resolution. The corrections were also performed for each experimental run (the duration of a run is typically 1–3 hours) to minimize the possible time-dependent response of detectors.

2. Event-plane resolution

The event-plane resolution for v_2 was evaluated by the two-subevent method. The event-plane resolution [35] is expressed as

$$\langle\cos(kn[\Psi_n - \Psi_{\rm RP}])\rangle = \frac{\sqrt{\pi}}{2\sqrt{2}}\chi_n e^{-\chi_n^2/4}\left[I_{(k-1)/2}\left(\frac{\chi_n^2}{4}\right) + I_{(k+1)/2}\left(\frac{\chi_n^2}{4}\right)\right], \tag{9}$$

where $\chi_n = v_n\sqrt{2M}$, M is the number of particles used to determine the event plane Ψ_n, I_k is the modified Bessel function of the first kind, and $k = 1$ for the second-harmonic BBC event plane.

To determine the event-plane resolution, we need to determine χ_n. Because the North and South BBCs have approximately the same η coverage, the event-plane resolution of each subdetector is expected to be the same. Thus, the subevent resolution for South and North event planes can be

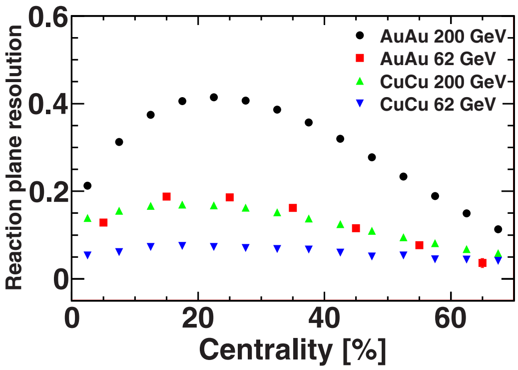

FIG. 4. (Color online) Second-order event-plane resolution vs centrality in Au + Au and Cu + Cu at 200 and 62.4 GeV. The event plane is measured by BBC.

expressed as

$$\left\langle \cos\left(2\left[\Psi_n^{\mathrm{S(N)}} - \Psi_{\mathrm{RP}}\right]\right)\right\rangle = \sqrt{\left\langle \cos\left(2\left[\Psi_n^{\mathrm{S}} - \Psi_n^{\mathrm{N}}\right]\right)\right\rangle}, \quad (10)$$

where $\Psi_n^{\mathrm{S(N)}}$ denotes the event plane determined by the South (North) BBC. Once the subevent resolution is obtained from Eq. (10), one can calculate χ_n^{sub} using Eq. (9). The χ_n for the full event can then be estimated by $\chi_n = \sqrt{2}\chi_n^{\mathrm{sub}}$. This is then substituted into Eq. (9) to give the full event resolution. Because the multiplicity of the full event is twice as large as that of the subevent, χ_n is proportional to $\sqrt{M}$.

Figure 4 shows the BBC North-South-combined resolution of the event plane as a function of the centrality in Au + Au and Cu + Cu at $\sqrt{s_{NN}} = 200$ and 62.4 GeV. The reaction-plane resolution and its uncertainties in Au + Au and Cu + Cu at 62.4 and 200 GeV are summarized in Table III.

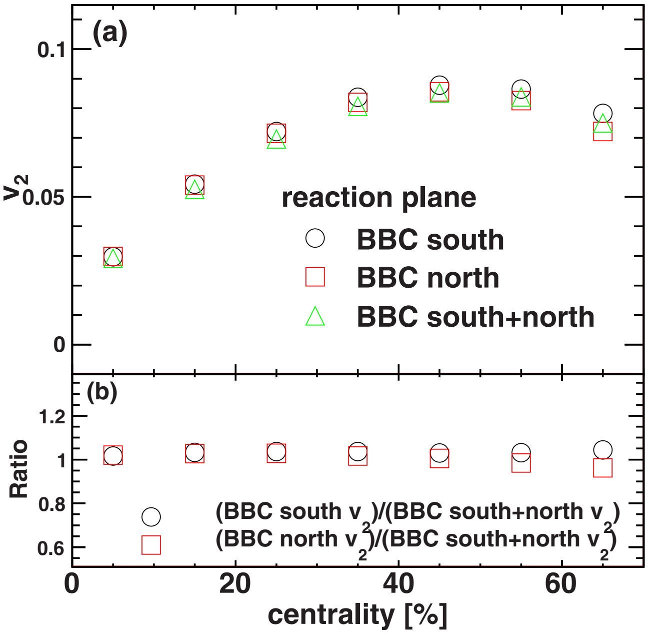

FIG. 5. (Color online) (a) v_2 vs centrality with three different reaction planes (BBC South, North, South-North combined) for Au + Au 200 GeV. (b) The ratio of v_2 with BBC South or North reaction plane to v_2 with South-North combined.

E. Systematic uncertainty for v_2

The sources of systematic uncertainty on the v_2 measurement include reaction-plane determination, the effects of matching cuts, the effects of the E/p cut, and occupancy effects for PID v_2. These are described below.

The systematic uncertainties owing to the reaction-plane determination were estimated by comparing the v_2 values extracted using three different reaction planes: the BBC North, BBC South, and BBC North-South combined. Figure 5(a)

TABLE III. Reaction-plane resolution for each centrality in Au + Au and Cu + Cu collisions at $\sqrt{s_{NN}} = 200$ and 62.4 GeV and its statistical contribution to the uncertainty on v_2. Note that centrality bins are 10% wide (0%–10%, 10%–20%, etc.) for Au + Au 62.4 GeV.

Centrality bin (%)	Au + Au 200 GeV		Au + Au 62.4 GeV		Cu + Cu 200 GeV		Cu + Cu 62.4 GeV	
	Resolution	Stat. uncert. for v_2 (%)	Resolution	Stat. uncert. for v_2 (%)	Resolution	Stat. uncert. for v_2 (%)	Resolution	Stat. uncert. for v_2 (%)
0–5	0.212	0.20	0.128	2.0	0.139	0.55	0.053	5.6
5–10	0.312	0.09			0.155	0.44	0.061	4.3
10–15	0.375	0.06	0.189	0.94	0.167	0.38	0.073	3.0
15–20	0.405	0.05			0.170	0.37	0.075	2.8
20–25	0.414	0.05	0.186	0.97	0.168	0.38	0.073	3.0
25–30	0.407	0.05			0.162	0.40	0.071	3.2
30–35	0.387	0.06	0.163	1.3	0.152	0.46	0.068	3.4
35–40	0.357	0.07			0.138	0.56	0.067	3.5
40–45	0.320	0.09	0.118	2.4	0.125	0.68	0.060	4.4
45–50	0.278	0.12			0.110	0.88	0.051	6.1
50–55	0.234	0.16	0.079	5.4	0.095	1.2	0.054	5.6
55–60	0.189	0.25			0.082	1.6	0.045	7.9
60–65	0.150	0.40	0.044	17.5	0.068	2.3	0.044	8.2
65–70	0.113	0.70			0.058	3.1	0.041	9.6

TABLE IV. Systematic uncertainty (%) of the reaction-plane determination for each data set and each centrality bin. These are obtained by taking the larger values away from unity of the ratio of v_2 with BBC North and South to v_2 with BBC North-South-combined.

Centrality bin (%)	Au + Au		Cu + Cu	
	200 GeV	62.4 GeV	200 GeV	64 GeV
0–10	2	3	3	14
10–20	3	2	2	9
20–30	4	2	2	6
30–40	4	7	2	2
40–50	3	7	2	3
50–60	3	5	2	5

shows v_2 vs centrality for three reaction planes (BBC South, North, South-North combined) for Au + Au 200 GeV. The panel (b) shows the ratio of v_2 with BBC North and South RP to v_2 with BBC North-South combined (default). The percentage systematic uncertainty was obtained by taking the largest values away from unity of these ratios. These uncertainties are summarized in Table IV for each data set and each centrality bin.

The default matching cuts for tracks projected to PC3 are $-2.5\sigma < (d\phi_{\rm PC3}$ and $dz_{\rm PC3}) < 2.5\sigma$. To obtain the systematic uncertainty from the dependence on these matching cuts, we examined different cut windows, e.g., $|d\phi_{\rm PC3}| < 1.0\sigma$ and $1.0\sigma < |d\phi_{\rm PC3}| < 2.5\sigma$, and compared v_2 values using these cuts to v_2 values from the default cut. The difference between v_2 values with these matching cuts determines the systematic uncertainties. Because the alternative cut windows have a smaller sample of data, we extracted the systematic uncertainty from the minimum bias event sample and used these for all centralities. Table V shows the matching systematic uncertainties.

The E/p cut can reject background from conversions, especially for high p_T tracks. The default cut, $E/p > 0.2$, was used for tracks with $p_T > 4$ GeV/c. To test the sensitivity to the value of the cut, we apply cuts of $E/p > 0.1, 0.2,$ and 0.3 cuts for tracks $3 < p_T < 4$ GeV/c; a lower momentum was used because we have more statistics there. The ratio of v_2 with different E/p cuts contributes to the systematic uncertainty. We obtained the systematic uncertainty owing to the E/p cut using the minimum bias event sample, because within the statistics we did not observe any centrality dependence for how v_2 changed with different E/p cuts. Table V lists the systematic uncertainties from the E/p cut.

TABLE VI. Systematic uncertainty (%) for v_2 of identified hadrons owing to the timing performance of the EMCal and TOF detectors. These are obtained by taking the difference between v_2 with EMCal and v_2 with TOF merging p_T and centrality bins.

Collision species	$\sqrt{s_{NN}}$ (GeV)	Identified hadron		
		π	K	p
Au + Au	62.4	2	4	6
Cu + Cu	200	3	5	6

Both EMCal and TOF detectors are used for PID. In the low-p_T region both detectors can be used, and the difference between v_2 measured with the EMCal and TOF, averaged across p_T, is used for the systematic uncertainty owing to timing performance. This includes the 1% uncertainty owing to background contributions in the PID. The values are summarized in Table VI. Note that the timing systematic uncertainty only affects the identified hadron results.

The values for v_2 can be impacted owing to finite occupancy which tends to lower the measured v_2. The magnitude of this effect has been estimated to be largest for central Au + Au collisions at 200 GeV as a reduction in v_2 for PID particles of approximately 0.0013 for the running conditions of the data presented here. This effect is independent of p_T. For different centrality and beam energies we take the systematic uncertainty on PID v_2 to linearly decrease with the average charged-particle multiplicity in those collisions.

IV. RESULTS FOR v_2 OF INCLUSIVE CHARGED HADRONS

In this section we describe the v_2 measurements and how they change as a function of collision energy and system size. We present the measured v_2 for inclusive charged particles in Au + Au and Cu + Cu collisions at 62.4 and 200 GeV. For 200 GeV, the v_2 results for $p_T < 5$ GeV/c are obtained by rebinning the data published in Refs. [7,24,36]. The new 200-GeV data published in this paper are v_2 results for $p_T > 5$ GeV/c. In addition, the 62.4-GeV Cu + Cu data are new results original in this paper.

The centrality selections of each collision system are as follows.

(1) Au + Au collisions at $\sqrt{s_{NN}} = 200$ GeV
    (i) Minimum bias: 0%–92%

TABLE V. Systematic uncertainty (%) of the matching and E/p cuts for each data set and each p_T bin for minimum bias event sample, which are obtained by taking the larger values of the ratio of v_2 with different matching cut to v_2 with the default matching cut.

p_T (GeV/c)	Au + Au 200 GeV Systematic uncertainty (%)		Au + Au 62.4 GeV Systematic uncertainty (%)		Cu + Cu 200 GeV Systematic uncertainty (%)		Cu + Cu 62.4 GeV Systematic uncertainty (%)	
	Matching cut	E/p cut	Matching cut	E/p cut	Matching cut	E/p cut	Matching cut	E/p cut
0.2–1.0	1	1	1	2	1	3	2	3
1.0–2.0	1	3	1	4	1	2	1	2
2.0–4.0	1	2	4	3	1	3	2	3

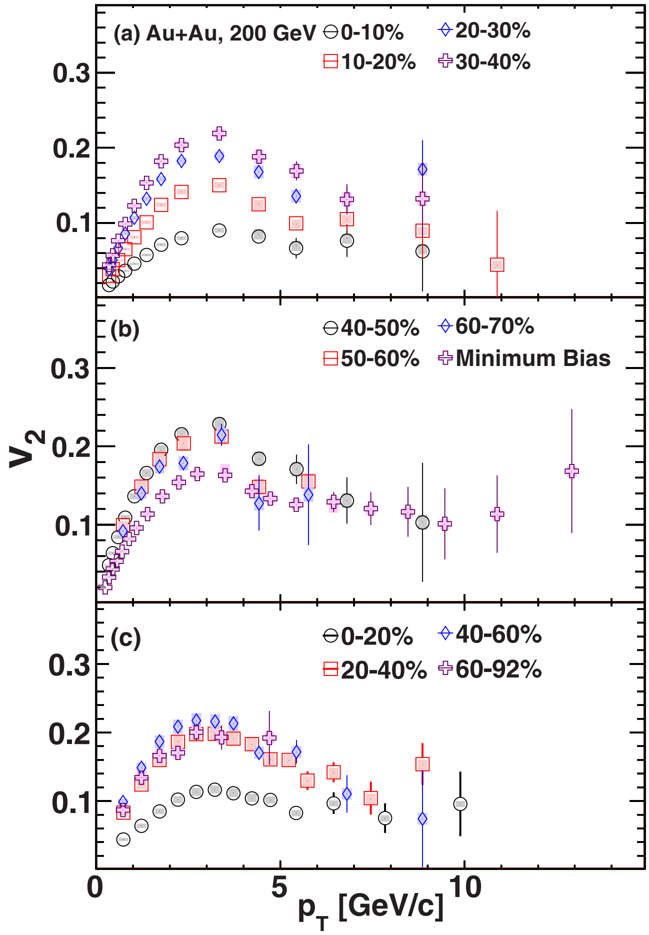

FIG. 6. (Color online) v_2 for inclusive charged hadrons in Au + Au at $\sqrt{s_{NN}} = 200$ GeV for the centralities indicated. The error bars show statistical uncertainties and the bands show systematic uncertainties. In many cases, the systematic uncertainties are smaller than the symbols.

    (ii) 10% steps: 0%–10%, 10%–20%, 20%–30%, 30%–40%, 40%–50%, 50%–60%
    (iii) 20% steps: 0%–20%, 20%–40%, 40%–60%
    (iv) Most peripheral bin: 60%–92%
(2) Au + Au collisions at $\sqrt{s_{NN}} = 62.4$ GeV
    (i) Minimum bias: 0%–83%
    (ii) 10% steps: 0%–10%, 10%–20%, 20%–30%, 30%–40%, 40%–50%
(3) Cu + Cu collisions at $\sqrt{s_{NN}} = 62.4$ and 200 GeV
    (i) Minimum bias: 0%–88%
    (ii) 10% steps: 0%–10%, 10%–20%, 20%–30%, 30%–40%, 40%–50%

A. v_2 vs p_T results for inclusive charged hadrons

1. Au + Au *at* $\sqrt{s_{NN}} = 200$ *GeV*

We analyzed 860×10^6 Au + Au collisions at 200 GeV collected during the 2003–04 experimental period, which is more than 20 times larger than the sample of events (30×10^6) analyzed from the 2001–02 experimental period [5]. Figure 6 shows the v_2 for inclusive charged hadrons in Au + Au collisions at 200 GeV.

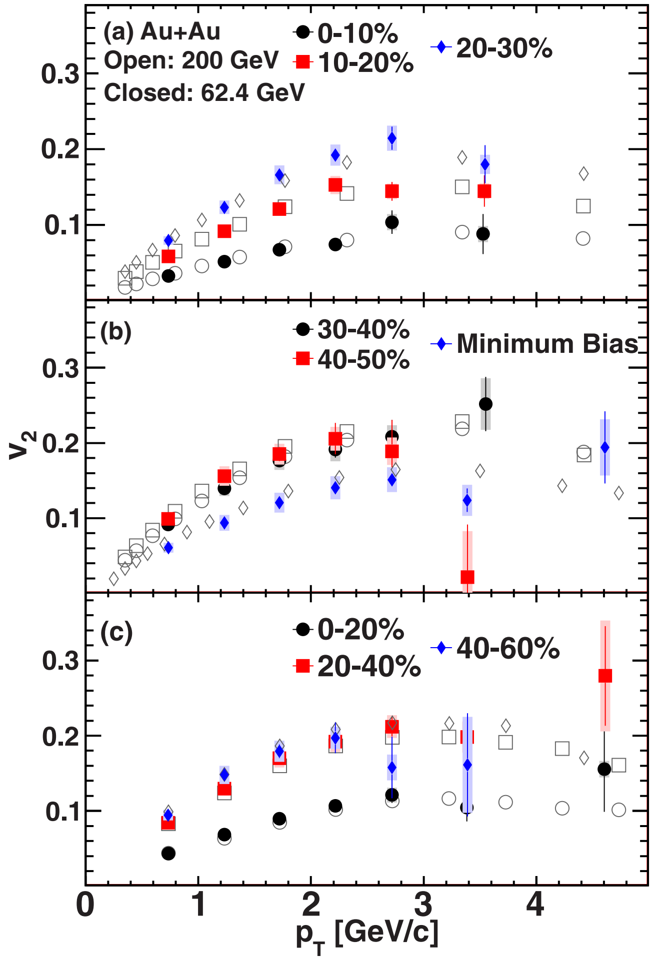

FIG. 7. (Color online) v_2 for inclusive charged hadrons in Au + Au at $\sqrt{s_{NN}} = 62.4$ and 200 GeV for the centralities indicated. The error bars show statistical uncertainties and the bands show systematic uncertainties. In many cases, the systematic uncertainties are smaller than the symbols.

2. Au + Au *at* $\sqrt{s_{NN}} = 62.4$ *GeV*

For Au + Au collisions at 62.4 GeV, 30×10^6 events were analyzed to study the dependence of v_2 on collision center-of-mass energy. The measured v_2 results from this collision system are shown in Fig. 7, together with the results from Au + Au 200-GeV collisions. The values of N_{part} are very similar at these two beam energies. We observe that the v_2 measurements for Au + Au collisions at 62.4 GeV are consistent with those for Au + Au at 200 GeV, within the combined statistical and systematic uncertainties.

3. Cu + Cu *at* $\sqrt{s_{NN}} = 200$ *and 62.4 GeV*

For Cu + Cu collisions at 62.4 GeV, 340×10^6 events were analyzed to study the dependence of v_2 on collision center-of-mass energy and system size. Figure 8 shows the v_2 results at 62.4 GeV in minimum bias events and 10% centrality

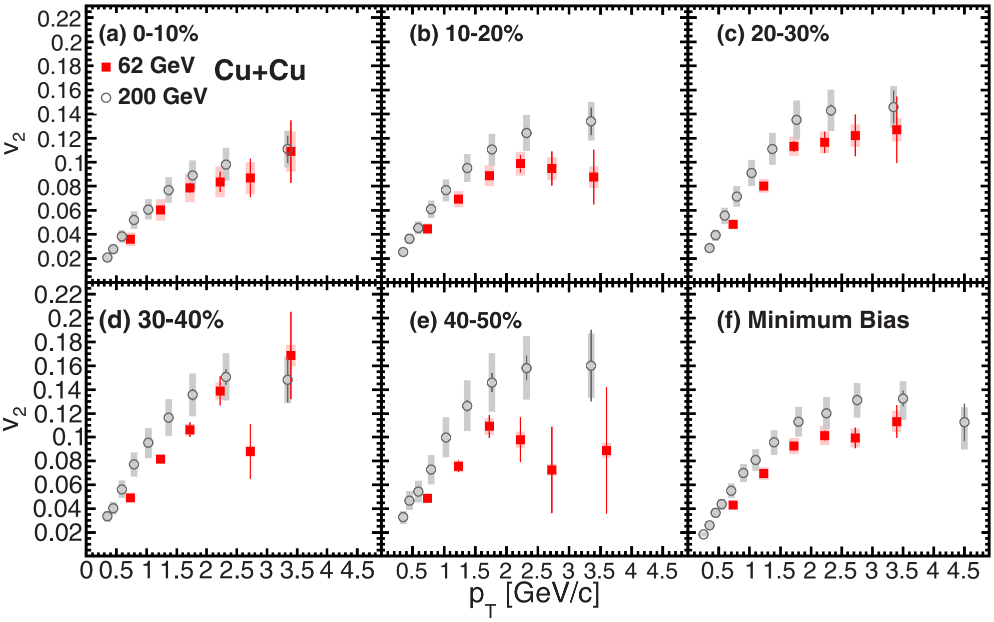

FIG. 8. (Color online) v_2 for inclusive charged hadrons in Cu + Cu at $\sqrt{s_{NN}} = 62.4$ GeV compared with 200 GeV [7] for the centralities indicated. The error bars show statistical uncertainties and the bands show systematic uncertainties. In many cases, the systematic uncertainties are smaller than the symbols.

selections. These are compared with Cu + Cu 200-GeV v_2 results [7]. The v_2 results for Cu + Cu collisions at 62.4 GeV are clearly smaller than those in 200-GeV collisions, especially at $p_T < 1.5$ GeV/c.

B. System comparisons

1. Centrality and collision energy dependence

An alternative view of these data is to make separate p_T selections and to plot v_2 in a given p_T range as a function of centrality and collision energy. Figure 9 presents the Au + Au data as a function of centrality, where triangles, boxes, and circles correspond to three p_T bins, 0.2–1.0, 1.0–2.0, and 2.0–4.0 GeV/c, respectively. The two different beam energies are presented by open and closed symbols for 62.4 and 200 GeV, respectively. The data confirm prior results that v_2 increases from central to midcentral collisions and then begins to decrease again towards peripheral collisions. The v_2 for Au + Au at 62.4 and 200 GeV agree to within statistical and systematic uncertainties for all measured centralities.

A similar v_2 comparison has been carried out by the STAR experiment, reaching even lower energies from $\sqrt{s_{NN}} = 7.7$ to 200 GeV [19]. Their results show that the v_2 (p_T) increases slightly from 7.7 up to 39 GeV, then saturates above 39 GeV.

Figure 10 shows the centrality dependence of v_2 for charged hadrons emitted at different p_T from Cu + Cu collisions at 62.4 and 200 GeV. The statistical uncertainties are larger owing to lower statistics for the Cu + Cu in the 62.4-GeV data sample. The measured v_2 values are lower at 62.4 GeV compared with 200 GeV.

We have made a comparison between the measured PHENIX v_2 and the previously published STAR v_2 measurement [20] in Cu + Cu collisions and found them to be generally consistent. For 200-GeV Cu + Cu the PHENIX v_2 are higher by about 10% in the 0%–10%, 10%–20%, 20%–30%, and 30%–40% centrality bins and higher by about 20% in 40%–50% bin; these differences are within statistical and systematic uncertainties of the PHENIX results in all cases. At 62.4 GeV the PHENIX v_2 is lower by approximately 10% in the 0%–40% bins and by 20% in 40%–50% bin. These differences are within statistical and systematic uncertainties in the 0%–20% bins, though they are roughly twice the statistical

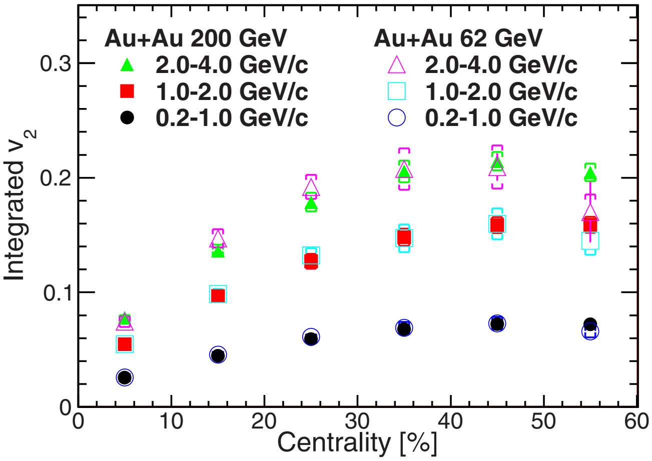

FIG. 9. (Color online) Comparison of integrated v_2 at $\sqrt{s_{NN}} =$ 62.4 and 200 GeV in Au + Au. Solid symbols indicate $\sqrt{s_{NN}} =$ 200 GeV and open symbols indicate $\sqrt{s_{NN}} = 62.4$ GeV. Ranges of p_T integrated are 0.2–1.0 (circles), 1.0–2.0 (squares), and 2.0–4.0 (triangles) GeV/c. The bars indicate the statistical uncertainties and the boxes indicate the systematic uncertainties. In many cases, the systematic uncertainties are smaller than the symbols.

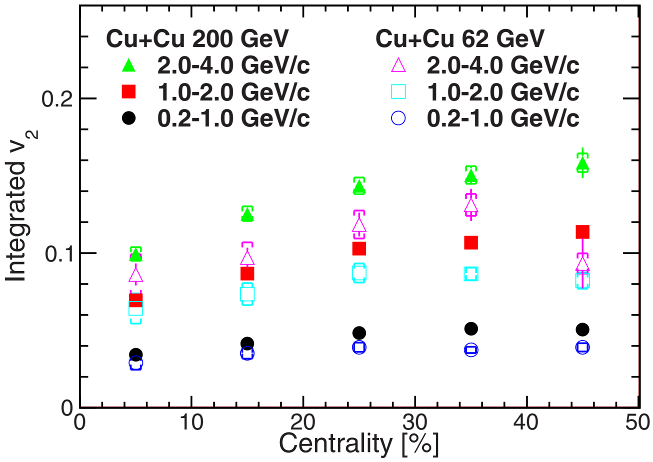

FIG. 10. (Color online) Comparison of integrated v_2 at $\sqrt{s_{NN}} =$ 62.4 and 200 GeV in Cu + Cu. Open symbols indicate $\sqrt{s_{NN}} =$ 62.4 GeV and solid symbols indicate $\sqrt{s_{NN}} = 200$ GeV. Ranges of p_T integrated are 0.2–1.0 (circles), 1.0–2.0 (squares), and 2.0–4.0 (triangles) GeV/c. The bars indicate the statistical uncertainties and the boxes indicate the systematic uncertainties. In many cases, the systematic uncertainties are smaller than the symbols.

and systematic uncertainties in 20%–50% bins, taking into account errors on the PHENIX measurement alone.

2. *Geometry dependence, eccentricity, and $N_{\rm part}$*

There are two ways to establish the extent to which v_2 changes with the system size: One is to change the collision centrality; the other is to change the colliding nuclei. As seen in Fig. 11, the measured v_2 in Cu + Cu collisions is smaller than that of Au + Au at a comparable $N_{\rm part}$.

Because ε is different between Au + Au and Cu + Cu collisions at the same $N_{\rm part}$, we can try to normalize v_2 by ε. In the bottom row of Fig. 11, v_2 normalized by ε is similar in magnitude for both Cu + Cu and Au + Au collisions. This confirms that the eccentricity normalization can account for the effect of the initial geometrical anisotropy [30]. The exception is that the Cu + Cu 62.4-GeV data falls below the other data. Note that the ratio v_2/ε also depends on centrality ($N_{\rm part}$) and that there is a similar rate of increase of v_2/ε with $N_{\rm part}$ for all three p_T bins: 0.2–1.0, 1.0–2.0, and 2.0–4.0 GeV/c. This pattern suggests the need for an additional normalization or scaling factor that depends on $N_{\rm part}$.

Figure 12 is a comparison of v_2 as a function of p_T for centrality classes that have approximately the same value of ε but with different values of $N_{\rm part}$. The average $N_{\rm part}$ is 166.6 for 20%–30%, 114.2 for 30%–40%, and 45.5 for 50%–60% in Au + Au collisions, while $N_{\rm part}$ is 73.6 for 10%–20%, 53.0 for 20%–30%, and 25.4 for 40%–50% in Cu + Cu collisions. It can be clearly seen that v_2 increases with $N_{\rm part}$ for similar ε.

3. *Participant $N_{\rm part}^{1/3}$ scaling*

We empirically explore using $N_{\rm part}^{1/3}$ as a potential scaling factor of v_2 in addition to ε. We draw on results with a different observable, namely that the Hanbury-Brown-Twiss source sizes at RHIC have been observed to scale with $N_{\rm part}^{1/3}$ [37]. Under the phenomenological assumption that $N_{\rm part}$ is proportional to the volume of hot, dense matter formed in

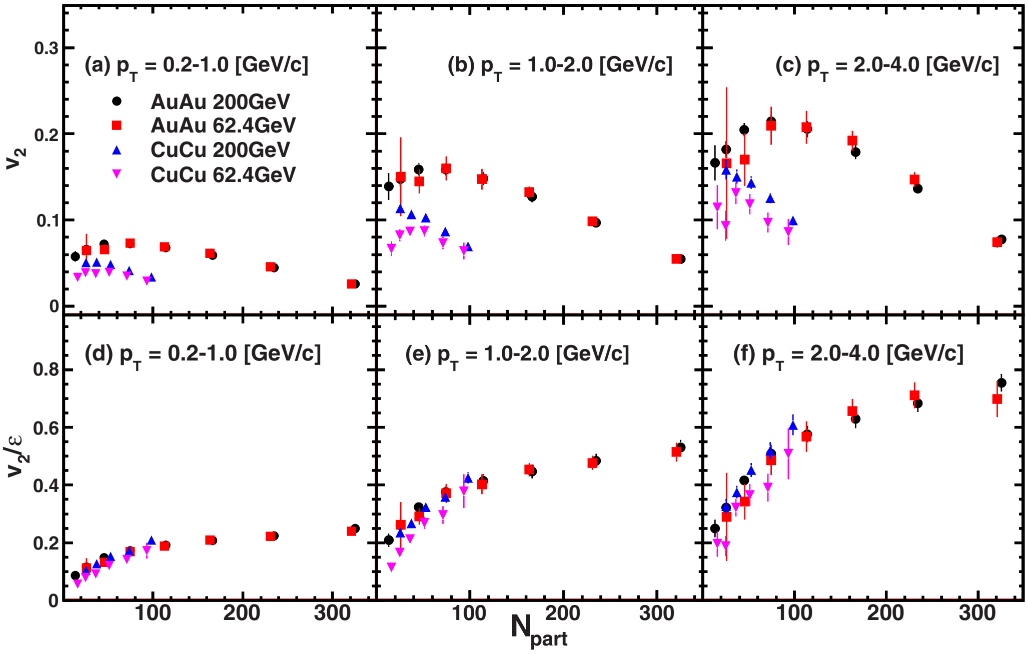

FIG. 11. (Color online) The top three panels show the comparison of integrated v_2 as a function of $N_{\rm part}$ and the bottom three panels show the comparison of the normalized v_2/ε vs $N_{\rm part}$ in both Au + Au and Cu + Cu at 200 and 62.4 GeV. The ranges of p_T integration are 0.2–1.0, 1.0–2.0, and 2.0–4.0 GeV/c from left to right and top to bottom panels, respectively. Both statistical and systematic uncertainties are included in the error bars.

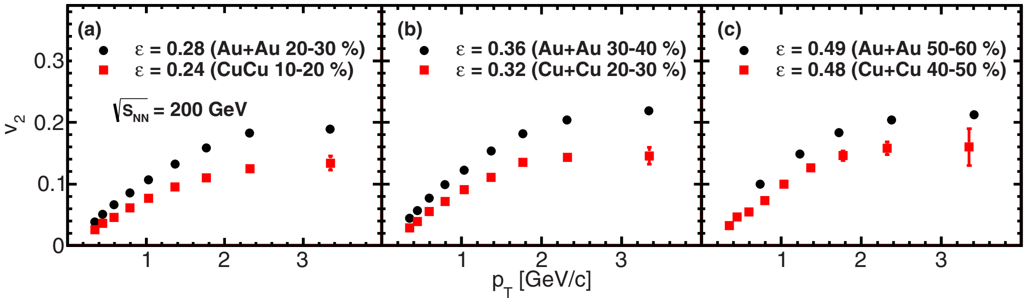

FIG. 12. (Color online) Comparison of v_2 (p_T) at 200 GeV for two example systems with different collision size (Au + Au or Cu + Cu) but approximately the same ε. Black symbols indicate Au + Au and red symbols indicate Cu + Cu. The average number of participants N_{part} is 166.6 for 20%–30%, 114.2 for 30%–40%, and 45.5 for 50%–60% at Au + Au collisions, and N_{part} is 73.6 for 10%–20%, 53.0 for 20%–30%, and 25.4 for 40%–50% at Cu + Cu collisions.

high-energy nuclear collisions, $N_{\text{part}}^{1/3}$ can be considered as a quantity proportional to a length scale.

Figure 13 plots $v_2/(\varepsilon \cdot N_{\text{part}}^{1/3})$ for integrated bins of $p_T = 0.2\text{–}1.0$, 1.0–2.0, and 2.0–4.0 GeV/c. This combination of two scaling factors works well; i.e., the scaled data are at comparable values, with the exception of the Cu + Cu data at 62.4 GeV, which deviate from this scaling, particularly at $N_{\text{part}} \leqslant 40$. That this empirical $v_2/(\varepsilon \cdot N_{\text{part}}^{1/3})$ scaling works well suggests that v_2 is determined by both the initial geometrical anisotropy and the number of participants.

Other scalings for the system size dependence have been suggested, particularly $1/S_{xy} dN/dy$ [38], where S_{xy} is the transverse area of the participant zone. Because dN/dy is proportional to N_{part} at a given beam energy and S_{xy} is approximately proportional to $(N_{\text{part}})^{2/3}$, $1/S_{xy} dN/dy$ is then proportional to $N_{\text{part}}^{1/3}$.

V. RESULTS FOR v_2 OF IDENTIFIED CHARGED HADRONS

More information can be obtained by examining v_2 for charged pions, kaons, and (anti) protons ($\pi/K/p$) each as a function of transverse momentum p_T. The charged particles are identified by TOF and EMCal and the data are presented for several classes of collision centrality

1. Au + Au collisions at $\sqrt{s_{NN}} = 62.4$ GeV
   - (i) 10%–40% (particles and antiparticles are measured separately)
   - (ii) 10% bins from 0% to 50% (particles and antiparticles are measured together)
2. Au + Au collisions at $\sqrt{s_{NN}} = 200$ GeV
   - (i) 0%–92% (particles and antiparticles are measured separately)
   - (ii) 10% bins from 0% to 50% (particles and antiparticles are measured together)
3. Cu + Cu collisions at $\sqrt{s_{NN}} = 200$ GeV
   - (i) 10% bins from 0% to 50% (particles and antiparticles are measured together)

Note that we do not present Cu + Cu 62.4-GeV data in this section because there were insufficient statistics to determine v_2 for identified particles.

A. Beam energy dependence

Figure 14 shows a summary of v_2 measurements of identified particles $\pi/K/p$ for three different data sets: Au + Au at 62.4 and 200 GeV and Cu + Cu at 200 GeV. Figure 15 shows the comparison between 62.4 and 200 GeV for Au + Au collisions. The measured v_2 in the 62.4- and 200-GeV data

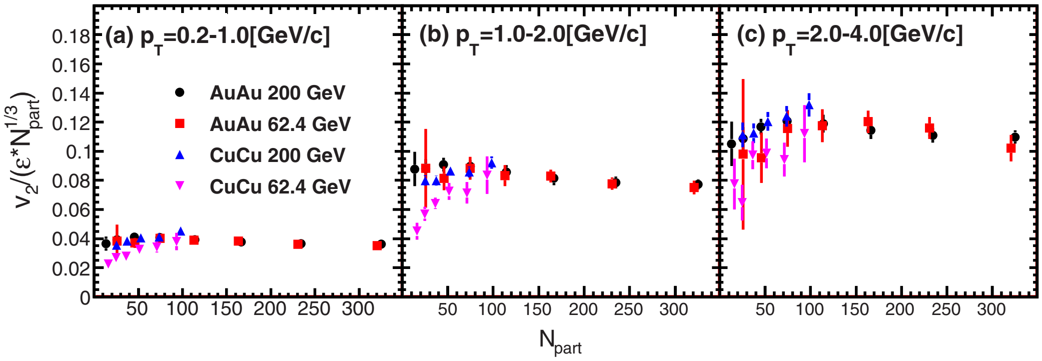

FIG. 13. (Color online) Comparison of integrated $v_2/(\varepsilon \cdot N_{\text{part}}^{1/3})$ as a function of N_{part} for two collision energies and two collision systems, Au + Au at 200 GeV, Au + Au at 62.4 GeV, Cu + Cu at 200 GeV, and Cu + Cu at 62.4 GeV. Ranges of p_T integration are 0.2–1.0, 1.0–2.0, and 2.0–4.0 GeV/c from left to right panels, respectively. All uncertainties from the measured v_2, ε, and N_{part} are included in the error bars.

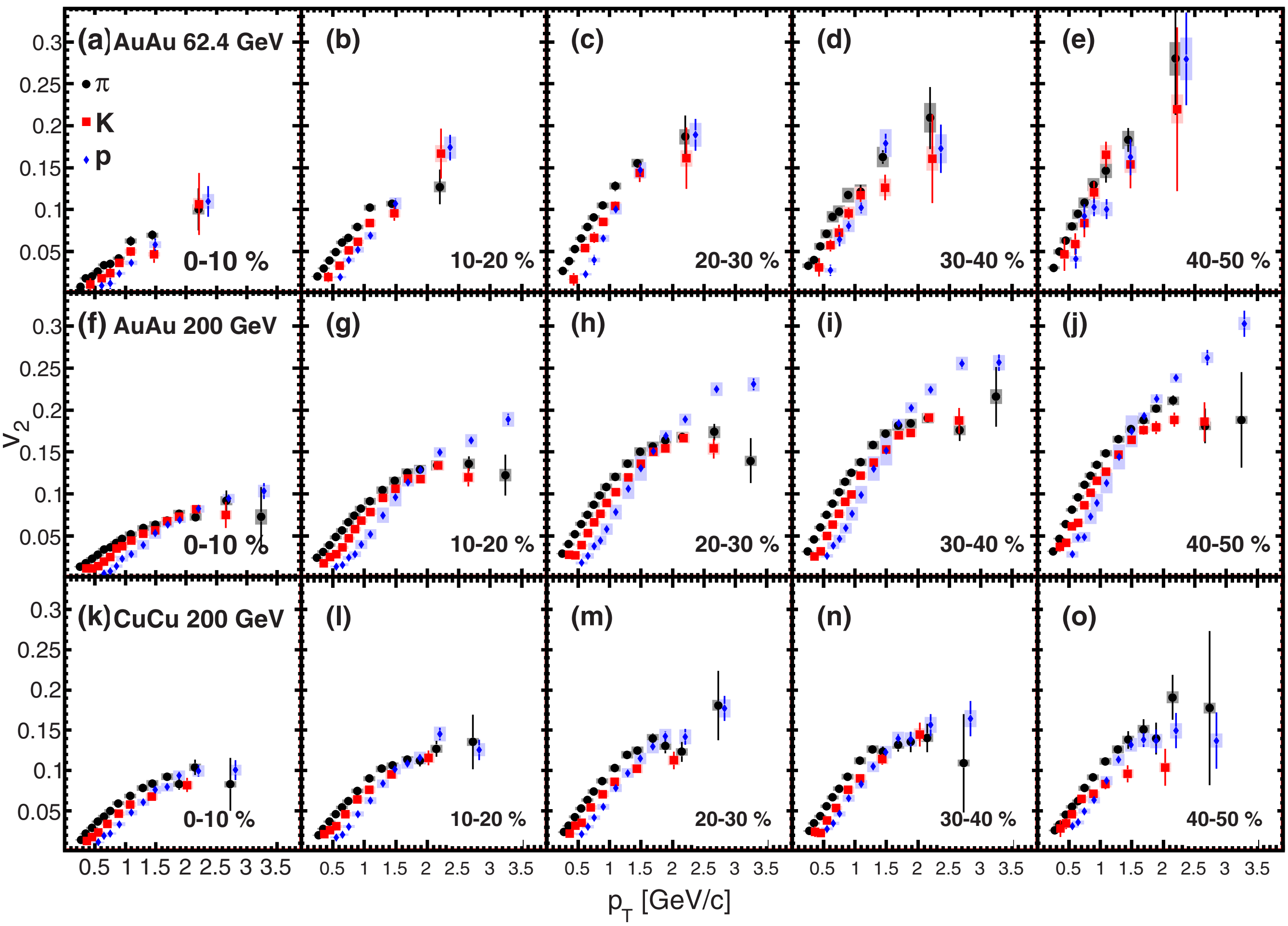

FIG. 14. (Color online) v_2 vs p_T for $\pi/K/p$ emitted from Au + Au at 62.4 and 200 GeV and Cu + Cu at 200-GeV collisions for the centralities indicated. The lines for each point indicate the statistical uncertainties, and the boxes are systematic uncertainties. In many cases, the systematic uncertainties are smaller than the symbols.

sets are consistent, within the systematic uncertainties, with the exception of proton v_2 at 62.4 GeV, which is slightly higher than at 200 GeV in the lower p_T region. These small differences could be caused by larger radial flow at higher $\sqrt{s_{NN}}$, especially for heavier particles such as protons.

The observation that the proton v_2 is larger at 62.4 GeV than at 200 GeV for Au + Au collisions is opposite to the earlier observation that inclusive charged v_2 at 62.4 GeV is lower than that at 200-GeV Cu + Cu. Therefore, the differences in lower v_2 for inclusive charged hadrons from Cu + Cu may be caused by different physics than the radial flow effect seen in Au + Au collisions.

B. Particle-antiparticle comparison

When we examine identified v_2 we combine opposite charged particles, e.g., $\pi^{\pm}$, to form π v_2. Prior results on

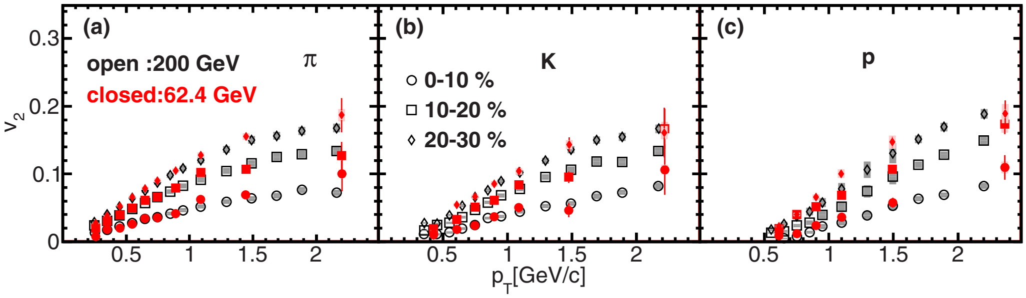

FIG. 15. (Color online) Comparison of v_2 between $\sqrt{s_{NN}} = 62.4$ and 200 GeV for $\pi/K/p$ emitted from 0%–10%, 10%–20%, and 20%–30% central Au + Au collisions. Both results for all species agree within the errors. The lines indicate the statistical uncertainties at each point and the boxes indicate the systematic uncertainties. In many cases, the systematic uncertainties are smaller than the symbols.

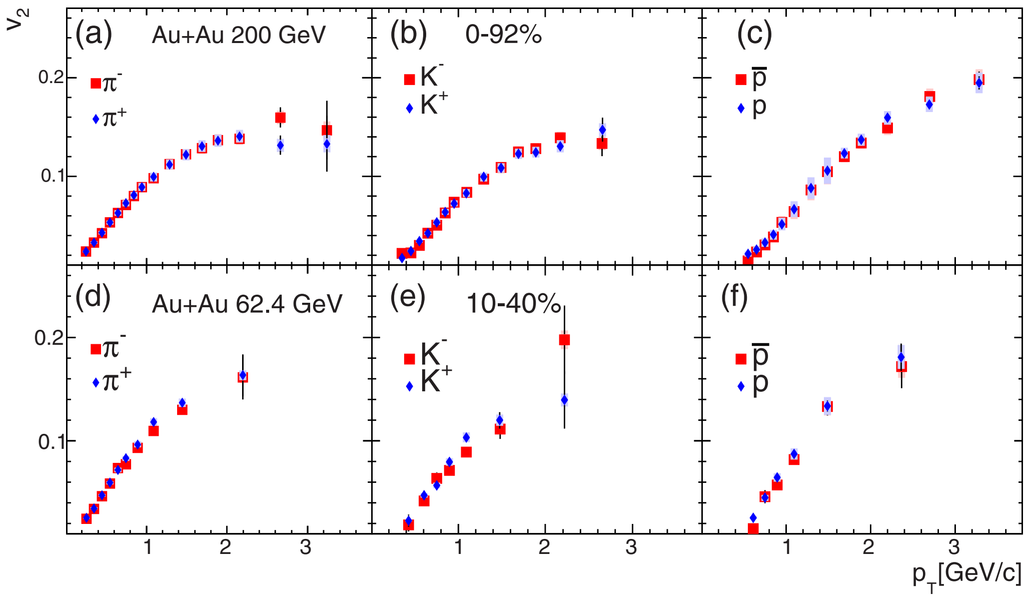

FIG. 16. (Color online) Comparison of the v_2 of particles and antiparticles for a minimum bias sample 0%–92% at 200 GeV and 10%–40% central at 62.4 GeV in Au + Au collisions. The lines for each point indicate the statistical uncertainties, and the boxes are systematic uncertainties. In many cases, the systematic uncertainties are smaller than the symbols.

the ratio of v_2 for antiparticles and particles can be found in Refs. [19,39]. In this section we compare the particle and antiparticle v_2 in Au + Au collisions at 200 and 62.4 GeV in wide centrality classes: a minimum bias sample (0%–92%) for 200-GeV data and 10%–40% for 62.4-GeV data. The first and second rows of plots in Fig. 16 present v_2 as a function of p_T for $\pi^{\pm}$, $\mathrm{K}^{\pm}$, p, and $\bar{\mathrm{p}}$ in Au + Au collisions at 200 and 62.4 GeV. The lines for each point are the statistical uncertainties and the boxes are systematic uncertainties.

At both 200 and 62.4 GeV, the the measured Au + Au v_2 values of particle and antiparticle are comparable to each other within uncertainty, though there is a possible indication of a small reduction of antiproton v_2 at lower p_T. When we combine particle and antiparticle v_2 we average over these differences.

C. Number of valence quark n_q scaling of v_2

The v_2 measurements of identified particles $\pi/K/p$ for three different data sets: Au + Au at 62.4- and 200-GeV collisions and Cu + Cu at 200-GeV collisions are replotted in Fig. 17 after scaling by the number of constituent quarks for both v_2 and p_T axes as shown. An alternative scaling is to use transverse kinetic energy. We define transverse kinetic energy as $KE_T = m_T - m$, where m is the mass of the hadron and $m_T = \sqrt{p_T^2 + m^2}$. The quark number scaled v_2 are shown as a function of KE_T/n_q for all three data sets in Fig. 18.

Note that at higher values, $KE_T/n_q > 0.7$, PHENIX has observed significant deviations from n_q scaling for Au + Au noncentral collisions [8]. Those higher KE_T results indicate that the azimuthal anisotropy of these high-KE_T particles are impacted by mechanisms such as parton-energy loss, jet chemistry, and/or different fragmentation functions. For comparison, at the LHC [17,18], v_2 does not scale well with the quark number and transverse kinetic energy of the hadron in any range of KE_T/n_q, with up to 40% deviations observed at low values of KE_T/n_q.

To quantify how well the number of quark scaling with KE_T works with the current data, we fit all the hadron species data in Fig. 18 with a common polynomial function for each centrality and colliding system. We divide the data by these fits to compare how close different hadron species are to the common scaled shape of v_2. Figure 19 shows these ratios as a function of KE_T/n_q for $\pi/K/p$ in Au + Au and Cu + Cu. Deviations from the fitted polynomial function are observed, especially with the high statistics data sets at 200-GeV Au + Au and 200-GeV Cu + Cu collisions. For Au + Au central collisions in the low-KE_T/n_q region ($KE_T/n_q < 0.1$ GeV), protons sit below the common scaling fit and rise above the fit at moderate KE_T/n_q. These deviations systematically change with centrality; i.e., the proton v_2 is smaller than pion v_2 at low KE_T/n_q in the most central Au + Au collisions at 200 GeV, while the proton v_2 becomes larger than pion v_2 in peripheral collisions. The proton v_2 is also larger than the pion v_2 at low KE_T/n_q in 200-GeV Cu + Cu peripheral collisions. The proton and pion v_2 become comparable in central Cu + Cu collisions. It is noted that the location where the proton and pion v_2 flows are comparable occurs at a similar number of participants N_{part} for Au + Au and Cu + Cu. This could be explained by an increase in radial flow as a function of the number of participants, which effectively reduces the proton v_2 relative to the pion v_2 for a given p_T [40].

For Cu + Cu collisions at 200 GeV, the bottom five panels of Figs. 17 and 18 show the v_2/n_q vs p_T/n_q and KE_T/n_q, respectively, for $\pi/K/p$ emitted from Cu + Cu collisions at 200 GeV for the five centrality bins: 0%–10%, 10%–20%, 20%–30%, 30%–40%, and 40%–50%. For the smaller system of Cu + Cu at 200 GeV (the bottom row of Fig. 18), quark

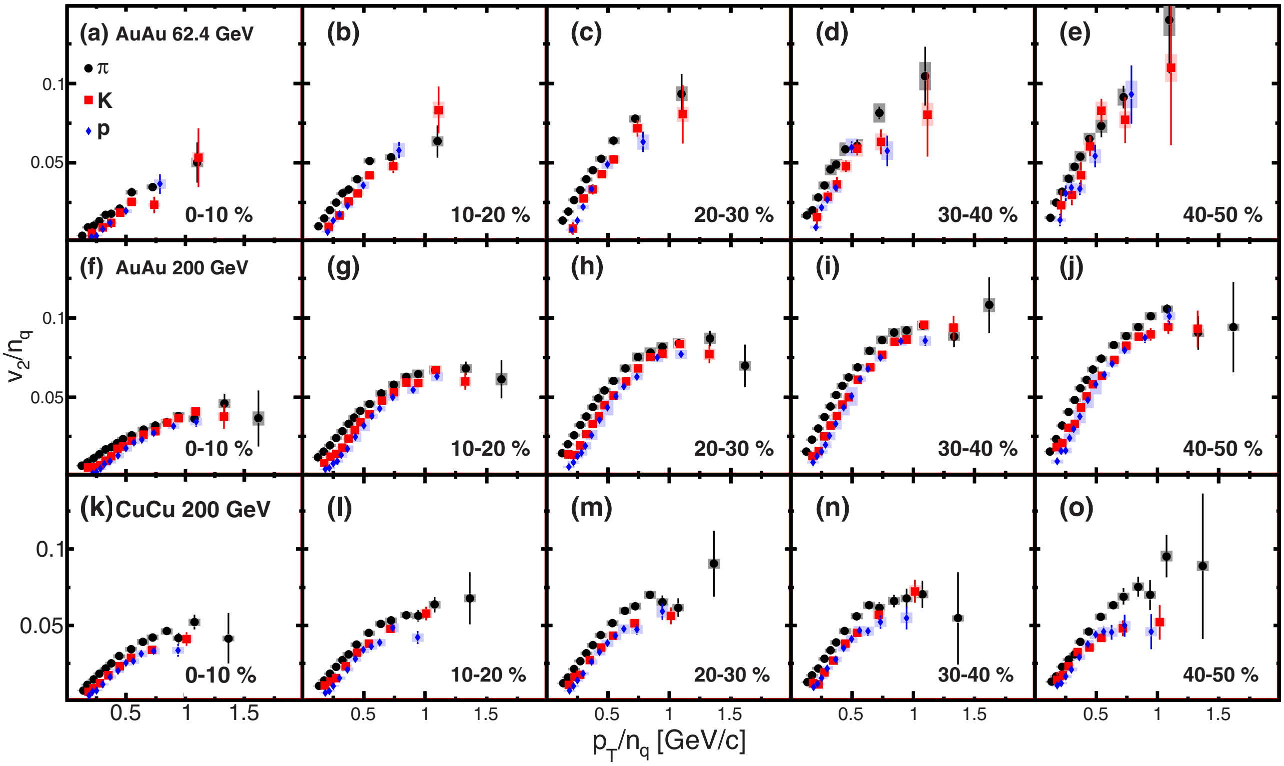

FIG. 17. (Color online) The ratio v_2/n_q vs p_T/n_q for $\pi/K/p$ emitted from Au + Au at 62.4- and 200-GeV collisions and Cu + Cu at 200-GeV collisions for the centralities indicated. The lines for each point indicate the statistical uncertainties, and the boxes are systematic uncertainties. In many cases, the systematic uncertainties are smaller than the symbols.

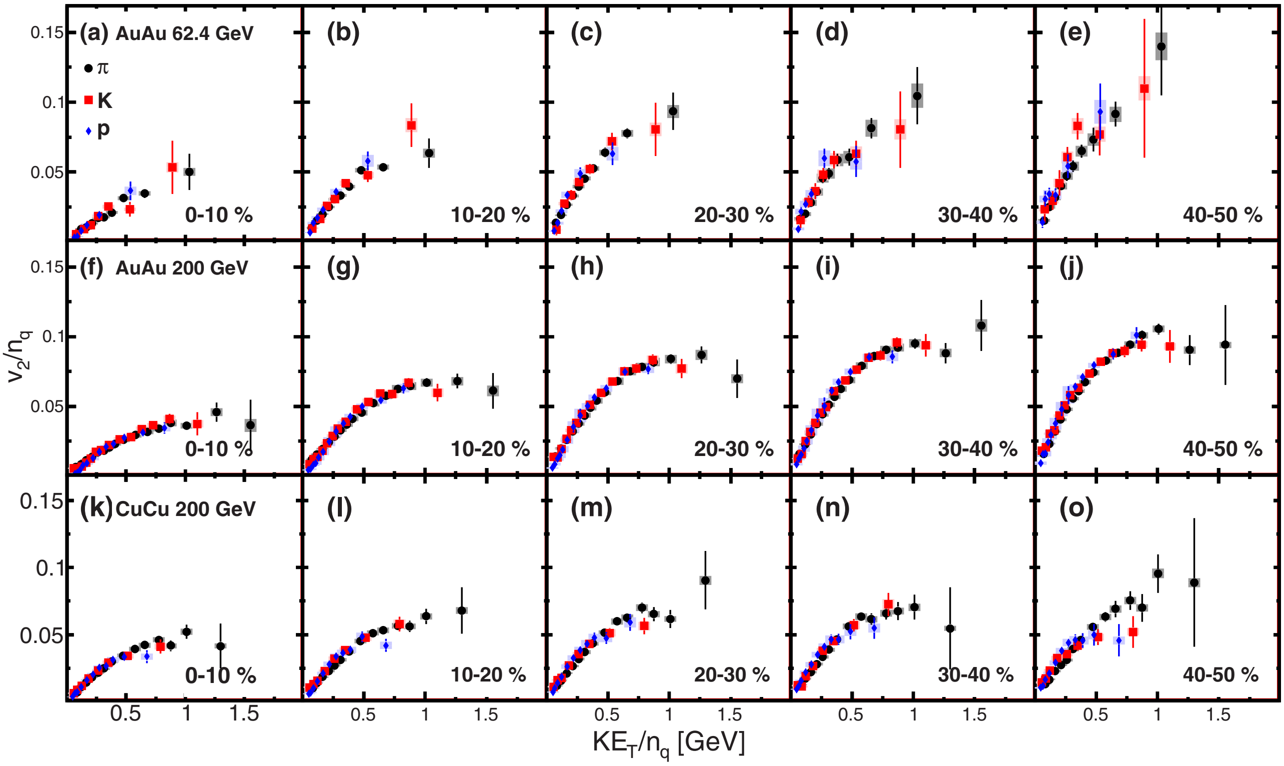

FIG. 18. (Color online) The ratio v_2/n_q vs KE_T/n_q for $\pi/K/p$ emitted from Au + Au at 62.4- and 200-GeV collisions and Cu + Cu at 200-GeV collisions for the centralities indicated. The lines for each point indicate the statistical uncertainties and the boxes are systematic uncertainties. In many cases, the systematic uncertainties are smaller than the symbols.

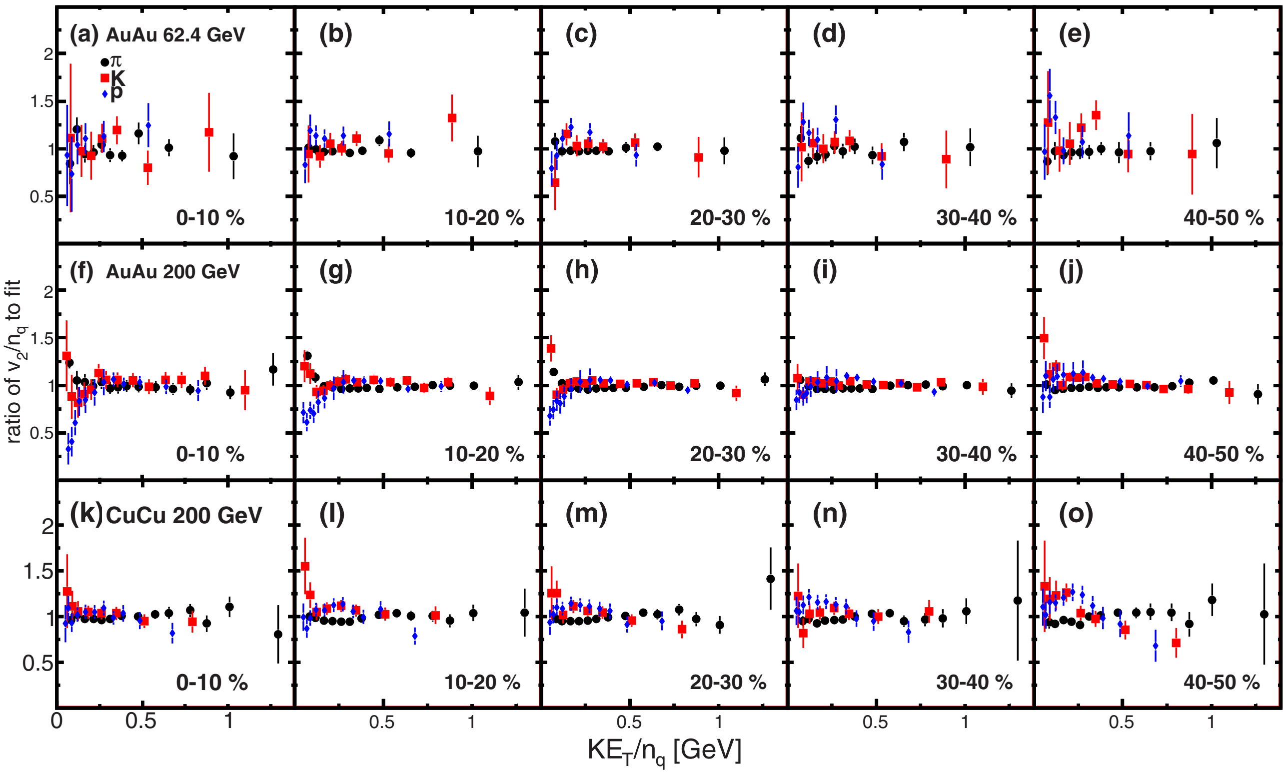

FIG. 19. (Color online) The ratio of v_2/n_q vs KE_T/n_q to the fit for $\pi/K/p$ emitted from Au + Au at 62.4- and 200-GeV collisions and Cu + Cu at 200-GeV collisions for the centralities indicated. The lines for each point indicate the statistical uncertainties.

number with KE_T scalings reduces the spread in v_2 values better than p_T scaling in Fig. 17, especially for the more central collisions between 0% and 40%. For peripheral Cu + Cu collisions, the number of quark scaling with KE_T does not work well. The deviation from n_q scaling seems to be largest at peripheral collisions, i.e., at 40%–50%, especially between pions and protons.

We examine in more detail the scaling at low KE_T in the 62.4-GeV data in stages. First, the left panel in Fig. 20 summarizes the unscaled v_2 data from 10%–40% central Au + Au collisions at 62.4 GeV. The v_2 values are broadly spread in their magnitude. A reduction in spread is observed in the right panel when n_q, the number of valence quarks, is used as a scaling. However, the scaled v_2 values do not collapse to a universal curve. Figure 21 does show a better scaling with KE_T/n_q.

Overall, the combined $n_q - KE_T$ scaling works well (typical deviations less than 20%) for $0.1 < KE_T/n_q < 1$ GeV, indicating that the elliptic collective motion is created at a level consistent with constituent quarks both at 62.4 GeV in Au + Au and at 200 GeV in Cu + Cu.

D. Universal v_2 scaling

We consider a universal v_2 scaling for all the v_2 measurements in this paper for identified hadrons between

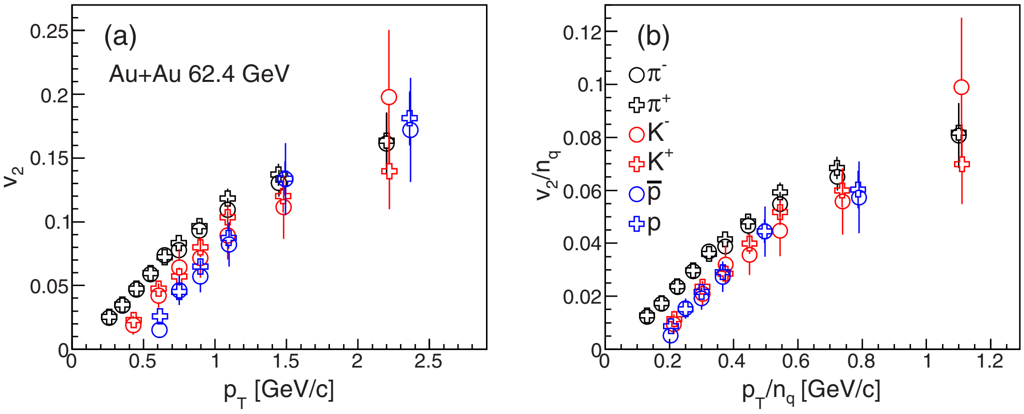

FIG. 20. (Color online) The left panel shows v_2 vs p_T; the right panel is the ratio v_2/n_q vs p_T/n_q for the indicated hadrons emitted from 10%–40% central Au + Au collisions in Au + Au at 62.4 GeV. The error bars include both systematic and statistical uncertainties.

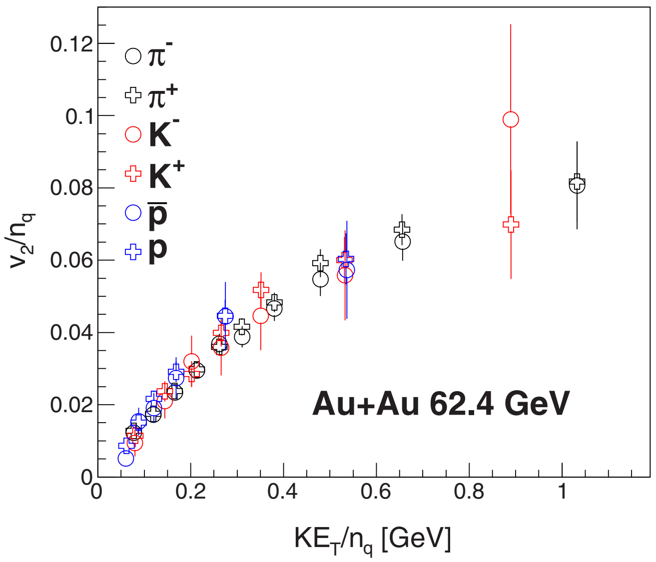

FIG. 21. (Color online) The ratio v_2/n_q vs KE_T/n_q for the indicated hadrons emitted from 10%–40% central Au + Au collisions at 62.4 GeV. The error bars include both systematic and statistical uncertainties.

$0.1 < KE_T/n_q < 1$ GeV. Within a given collision system, i.e., each centrality bin for each set of Au + Au and Cu + Cu collisions, we first apply quark number n_q scaling and KE_T scaling. Then we apply the eccentricity normalization and $N_{\rm part}^{1/3}$ scaling for each colliding system. Because we have observed that v_2 saturates with beam energy between 62 and 200 GeV, we do not apply any scaling with beam energy. The v_2 data with the four factors applied (quark number scaling, KE_T scaling, eccentricity normalization, and $N_{\rm part}^{1/3}$ scaling) are shown as a function of KE_T/n_q in Fig. 22, which includes data from Au + Au at 200 GeV, Au + Au at 62.4 GeV, and Cu + Cu at 200 GeV at five centrality bins over 0%–50% in 10% steps for each system. There are 45 v_2 data sets in total. The combined data are fit with a single third-order polynomial, producing a $\chi^2/NDF = 1034/490 = 2.11$ (including both statistical and systematic uncertainties). Note that there is no Cu + Cu 62.4-GeV data in Fig. 22, because there were insufficient statistics to determine v_2 for identified particles. If we apply the $N_{\rm coll}^{1/3}$ scaling to the same data sets instead of $N_{\rm part}^{1/3}$ scaling, we obtain $\chi^2/NDF = 2643/490 = 5.39$. Therefore, $N_{\rm part}^{1/3}$ is a better scaling factor than $N_{\rm coll}^{1/3}$. As we mentioned Sec. V C, there are some deviations from the quark number and KE_T scalings; therefore, this $N_{\rm part}^{1/3}$ normalized curve is not perfectly a single line. Further investigation of these deviations would require higher precision measurements.

VI. SUMMARY AND CONCLUSION

We have measured the strength of the elliptic anisotropy, v_2, for inclusive charged hadrons and identified charged hadrons ($\pi/K/p$) in Au + Au and Cu + Cu collisions at $\sqrt{s_{NN}} = 200$ and 62.4 GeV to study the dependence of v_2 on collision energy, species and centrality. Results of this systematic study reveal the following features. Comparisons between 200- and 62.4-GeV collisions demonstrate that v_2 as a function of p_T does not depend on beam energy in Au + Au. In Cu + Cu, the v_2 at 62.4 GeV is slightly lower than that at 200 GeV.

One possibility for the lower v_2 values at 62.4 GeV in Cu + Cu is less complete thermalization in small systems at lower beam energies. At least two types of theoretical models have been used to investigate the question of incomplete thermalization for systems formed at RHIC. Borghini argues that because v_2/ε depends on dN/dy [41], the systems formed at RHIC are not fully thermalized during the time when v_2 develops. Borghini argues that this dN/dy dependence can be interpreted as dependence on a Knudsen number representing incomplete thermalization. Recent hydrodynamical models that include shear viscosity and initial fluctuations [11–13]

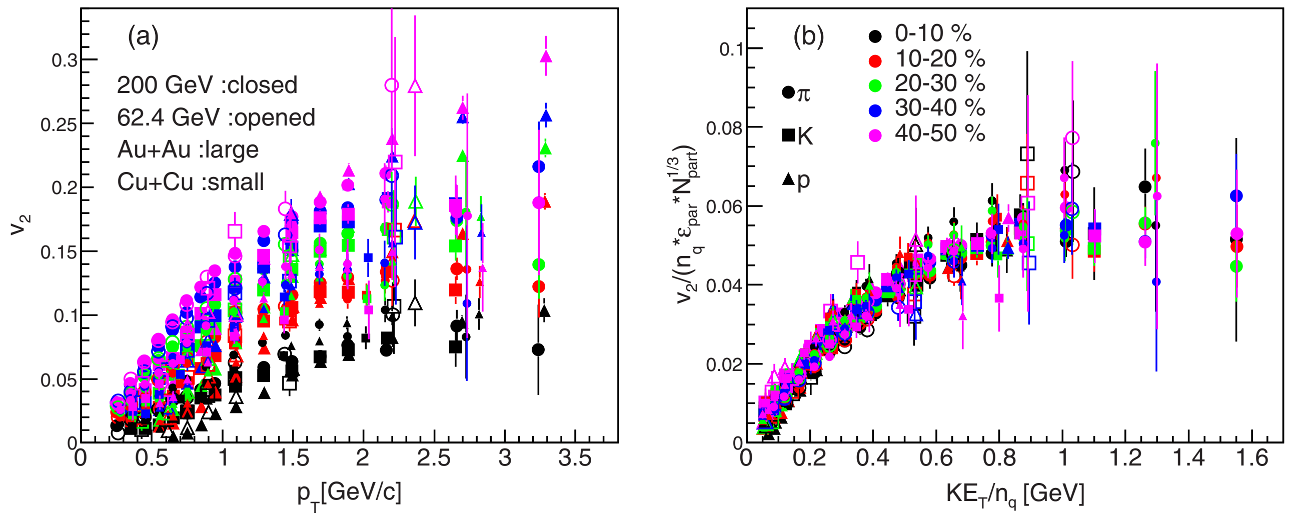

FIG. 22. (Color online) The left panel shows v_2 vs p_T and the right panel shows $v_2/(\varepsilon \cdot N_{\rm part}^{1/3} \cdot n_q)$ vs KE_T/n_q for $\pi/K/p$ in Au + Au at 200 GeV, in Au + Au at 62.4 GeV, and in Cu + Cu at 200 GeV for five centrality bins over 0%–50% in 10% steps for each system. There are 45 data sets in each panel.

effectively include nonequilibrium effects through the finite viscosity. Using a different nonequilibrium approach, microscopic transport models [42] solve the relativistic Boltzmann equation. Both the viscous hydrodynamical and the Boltzmann transport models can be tested with our two observations that the v_2 at Cu + Cu at 62.4 GeV is slightly lower than that at 200 GeV and that the measured universal scaling breaks down in peripheral Cu + Cu.

For various hadron species the measured v_2 results as a function of p_T are well scaled by quark number. Interestingly, it appears that this scaling holds also for higher orders in azimuthal anisotropy [43]. The KE_T scaling performs better than p_T scaling, particularly in the intermediate transverse momentum region ($p_T = 1$–4 GeV/c). This scaling property suggests that the matter flows with quarklike degrees of freedom and therefore is consistent with the formation of QGP matter [7]. A small deviation from KE_T scaling can be seen for both Au + Au and Cu + Cu collisions, and this deviation depends on the number of participants $N_{\rm part}$. This deviation might indicate a restricted region where KE_T scaling works well, possibly dependent on the strength of the radial flow.

For both Au + Au to Cu + Cu collisions, we confirm that v_2 can be normalized by participant eccentricity (ε) [30]. This indicates that the effect of initial geometrical anisotropy can be partially removed by eccentricity normalization. However, v_2 normalized by ε still depends on $N_{\rm part}$, v_2 is not fully determined by ε alone and we have empirically found that v_2/ε is proportional to $N_{\rm part}^{1/3}$. The initial participant size $N_{\rm part}^{1/3}$, is related to a length scale or an expansion time scale. Taking into account all scalings and normalization, the data "$v_2/n_q/\varepsilon/N_{\rm part}^{1/3}$ vs KE_T/n_q" lie on a universal curve for $0.1 < KE_T/n_q < 1$ GeV.

ACKNOWLEDGMENTS

We thank the staff of the Collider-Accelerator and Physics Departments at Brookhaven National Laboratory and the staff of the other PHENIX participating institutions for their vital contributions. We acknowledge support from the Office of Nuclear Physics in the Office of Science of the Department of Energy, the National Science Foundation, Abilene Christian University Research Council, Research Foundation of SUNY, and Dean of the College of Arts and Sciences, Vanderbilt University (USA); Ministry of Education, Culture, Sports, Science, and Technology, and the Japan Society for the Promotion of Science (Japan); Conselho Nacional de Desenvolvimento Científico e Tecnológico and Fundação de Amparo à Pesquisa do Estado de São Paulo (Brazil); Natural Science Foundation of China (P. R. China), Ministry of Education, Youth and Sports (Czech Republic); Centre National de la Recherche Scientifique, Commissariat à l'Énergie Atomique, and Institut National de Physique Nucléaire et de Physique des Particules (France); Bundesministerium für Bildung und Forschung, Deutscher Akademischer Austausch Dienst, and Alexander von Humboldt Stiftung (Germany); National Science Fund, OTKA, Károly Róbert University College, and the Ch. Simonyi Fund (Hungary); Department of Atomic Energy (India), Israel Science Foundation (Israel); National Research Foundation and WCU program of the Ministry Education Science and Technology (Korea); Ministry of Education and Science, Russian Academy of Sciences, Federal Agency of Atomic Energy (Russia); VR and Wallenberg Foundation (Sweden); the US Civilian Research and Development Foundation for the Independent States of the Former Soviet Union; the US-Hungarian NSF-OTKA-MTA; and the US-Israel Binational Science Foundation.

[1] K. Adcox *et al.* (PHENIX Collaboration), Formation of dense partonic matter in relativistic nucleus-nucleus collisions at RHIC: Experimental evaluation by the PHENIX Collaboration, Nucl. Phys. A **757**, 184 (2005).

[2] J. Adams *et al.* (STAR Collaboration), Experimental and theoretical challenges in the search for the quark gluon plasma: The STAR Collaboration's critical assessment of the evidence from RHIC collisions, Nucl. Phys. A **757**, 102 (2005).

[3] B. B. Back *et al.* (PHOBOS Collaboration), The PHOBOS perspective on discoveries at RHIC, Nucl. Phys. A **757**, 28 (2005).

[4] I. Arsene *et al.* (BRAHMS Collaboration), Quark gluon plasma and color glass condensate at RHIC? The Perspective from the BRAHMS experiment, Nucl. Phys. A **757**, 1 (2005).

[5] S. S. Adler *et al.* (PHENIX Collaboration), Elliptic Flow of Identified Hadrons in Au+Au Collisions at $\sqrt{s_{NN}} = 200$ GeV, Phys. Rev. Lett. **91**, 182301 (2003).

[6] M. Bleicher and H. Stoecker, Anisotropic flow in ultrarelativistic heavy ion collisions, Phys. Lett. B **526**, 309 (2002).

[7] A. Adare *et al.* (PHENIX Collaboration), Scaling Properties of Azimuthal Anisotropy in Au+Au and Cu+Cu Collisions at $\sqrt{s_{NN}} = 200$ GeV, Phys. Rev. Lett. **98**, 162301 (2007).

[8] A. Adare *et al.* (PHENIX Collaboration), Deviation from quark-number scaling of the anisotropy parameter v_2 of pions, kaons, and protons in Au+Au collisions at $\sqrt{s_{NN}} = 200$ GeV, Phys. Rev. C **85**, 064914 (2012).

[9] U. Heinz and R. Snellings, Collective flow and viscosity in relativistic heavy-ion collisions, Annu. Rev. Nucl. Part. Sci. **63**, 123 (2013).

[10] J.-Y. Ollitrault, Anisotropy as a signature of transverse collective flow, Phys. Rev. D **46**, 229 (1992).

[11] H. Niemi, G. S. Denicol, P. Huovinen, E. Molnar, and D. H. Rischke, Influence of a temperature-dependent shear viscosity on the azimuthal asymmetries of transverse momentum spectra in ultrarelativistic heavy-ion collisions, Phys. Rev. C **86**, 014909 (2012).

[12] H. Song, S. A. Bass, U. Heinz, T. Hirano, and C. Shen, Hadron spectra and elliptic flow for 200 A GeV Au+Au collisions from viscous hydrodynamics coupled to a Boltzmann cascade, Phys. Rev. C **83**, 054910 (2011); **86**, 059903(E) (2012).

[13] R. A. Soltz, I. Garishvili, M. Cheng, B. Abelev, A. Glenn, J. Newby, L. A. Linden Levy, and S. Pratt, Constraining the initial temperature and shear viscosity in a hybrid hydrodynamic model of $\sqrt{s_{NN}} = 200$ GeV Au+Au collisions using pion spectra, elliptic flow, and femtoscopic radii, Phys. Rev. C **87**, 044901 (2013).

[14] K Aamodt *et al.* (ALICE Collaboration), Charged-Particle Multiplicity Density at Mid-rapidity in Central Pb-Pb

Collisions at $\sqrt{s_{NN}} = 2.76$ TeV, Phys. Rev. Lett. **105**, 252301 (2010).
[15] G. Aad *et al.* (ATLAS Collaboration), Measurement of the azimuthal anisotropy for charged particle production in $\sqrt{s_{NN}} = 2.76$ TeV lead-lead collisions with the ATLAS detector, Phys. Rev. C **86**, 014907 (2012).
[16] S. Chatrchyan *et al.* (CMS Collaboration), Measurement of the elliptic anisotropy of charged particles produced in PbPb collisions at $\sqrt{s_{NN}} = 2.76$ TeV, Phys. Rev. C **87**, 014902 (2013).
[17] B. Abelev *et al.* (ALICE Collaboration), Anisotropic flow of charged hadrons, pions and (anti-)protons measured at high transverse momentum in Pb-Pb collisions at $\sqrt{s_{NN}} = 2.76$ TeV, Phys. Lett. B **719**, 18 (2013).
[18] B. B. Abelev *et al.* (ALICE Collaboration), Elliptic flow of identified hadrons in Pb-Pb collisions at $\sqrt{s_{NN}} = 2.76$ TeV, J. High Energy Phys. 06 (2015) 190.
[19] L. Adamczyk *et al.* (STAR Collaboration), Elliptic flow of identified hadrons in Au+Au collisions at $\sqrt{s_{NN}} = 7.7$-62.4 GeV, Phys. Rev. C **88**, 014902 (2013).
[20] B. I. Abelev *et al.* (STAR Collaboration), Charged and strange hadron elliptic flow in Cu+Cu collisions at $\sqrt{s_{NN}} = 62.4$ and 200 GeV, Phys. Rev. C **81**, 044902 (2010).
[21] A. Adare *et al.* (PHENIX Collaboration), Quadrupole Anisotropy in Dihadron Azimuthal Correlations in Central d + Au Collisions at $\sqrt{s_{NN}} = 200$ GeV, Phys. Rev. Lett. **111**, 212301 (2013).
[22] V. Khachatryan *et al.* (CMS Collaboration), Observation of long-range near-side angular Correlations in proton-proton collisions at the LHC, J. High Energy Phys. 09 (2010) 091.
[23] S. Chatrchyan *et al.* (CMS Collaboration), Observation of long-range near-side angular correlations in proton-lead collisions at the LHC, Phys. Lett. B **718**, 795 (2013).
[24] S. Afanasiev *et al.* (PHENIX Collaboration), Systematic studies of elliptic flow measurements in Au+Au collisions at $\sqrt{s} = 200$ GeV, Phys. Rev. C **80**, 024909 (2009).
[25] K. Adcox *et al.* (PHENIX Collaboration), PHENIX detector overview, Nucl. Instrum. Methods Phys. Res., Sec. A **499**, 469 (2003).
[26] M. Aizawa *et al.* (PHENIX Collaboration), PHENIX central arm particle ID detectors, Nucl. Instrum. Methods Phys. Res., Sec. A **499**, 508 (2003).
[27] K. Adcox *et al.* (PHENIX Collaboration), Construction and performance of the PHENIX pad chambers, Nucl. Instrum. Methods Phys. Res., Sec. A **497**, 263 (2003).
[28] L. Aphecetche *et al.* (PHENIX Collaboration), PHENIX calorimeter, Nucl. Instrum. Methods Phys. Res., Sec. A **499**, 521 (2003).
[29] S. S. Adler *et al.* (PHENIX Collaboration), Systematic studies of the centrality and $\sqrt{s_{NN}}$ dependence of the $dE_T/d\eta$ and $dN_{ch}/d\eta$ in heavy ion collisions at mid-rapidity, Phys. Rev. C **71**, 034908 (2005).
[30] B. Alver *et al.* (PHOBOS Collaboration), System Size, Energy, Pseudorapidity, and Centrality Dependence of Elliptic Flow, Phys. Rev. Lett. **98**, 242302 (2007).
[31] M. L. Miller, K. Reygers, S. J. Sanders, and P. Steinberg, Glauber modeling in high energy nuclear collisions, Annu. Rev. Nucl. Part. Sci. **57**, 205 (2007).
[32] J. T. Mitchell *et al.* (PHENIX Collaboration), Event reconstruction in the PHENIX central arm spectrometers, Nucl. Instrum. Methods Phys. Res., Sec. A **482**, 491 (2002).
[33] S. S. Adler *et al.* (PHENIX Collaboration), High p_T charged hadron suppression in Au + Au collisions at $\sqrt{s_{NN}} = 200$ GeV, Phys. Rev. C **69**, 034910 (2004).
[34] S. S. Adler *et al.* (PHENIX Collaboration), Jet structure from dihadron correlations in d+Au collisions at $\sqrt{s_{NN}} = 200$ GeV, Phys. Rev. C **73**, 054903 (2006).
[35] A. M. Poskanzer and S. A. Voloshin, Methods for analyzing anisotropic flow in relativistic nuclear collisions, Phys. Rev. C **58**, 1671 (1998).
[36] A. Adare *et al.* (PHENIX Collaboration), Elliptic and Hexadecapole Flow of Charged Hadrons in Au+Au Collisions at $\sqrt{s_{NN}} = 200$ GeV, Phys. Rev. Lett. **105**, 062301 (2010).
[37] S. Afanasiev *et al.* (PHENIX Collaboration), Kaon Interferometric Probes of Space-Time Evolution in Au+Au Collisions at $\sqrt{s_{NN}} = 200$ GeV, Phys. Rev. Lett. **103**, 142301 (2009).
[38] C. Adler *et al.* (STAR Collaboration), Elliptic flow from two and four particle correlations in Au+Au collisions at $\sqrt{s_{NN}} = 130$ GeV, Phys. Rev. C **66**, 034904 (2002).
[39] B. I. Abelev *et al.* (STAR Collaboration), Mass, quark-number, and $\sqrt{s_{NN}}$ dependence of the second and fourth flow harmonics in ultra-relativistic nucleus-nucleus collisions, Phys. Rev. C **75**, 054906 (2007).
[40] S. A. Voloshin, A. M. Poskanzer, and R. Snellings, Collective phenomena in non-central nuclear collisions, arXiv:0809.2949.
[41] N. Borghini, Hints of incomplete thermalization in RHIC data, Eur. Phys. J. A **29**, 27 (2006).
[42] J. Uphoff, F. Senzel, O. Fochler, C. Wesp, Z. Xu, and C. Greiner, Elliptic Flow and Nuclear Modification Factor in Ultrarelativistic Heavy-Ion Collisions within a Partonic Transport Model, Phys. Rev. Lett. **114**, 112301 (2015).
[43] A. Adare *et al.* (PHENIX Collaboration), Measurement of the higher-order anisotropic flow coefficients for identified hadrons in Au+Au collisions at $\sqrt{s_{NN}} = 200$ GeV, arXiv:1412.1038.